



UNIVERSITY  
OF TRENTO

---

DIPARTIMENTO DI INGEGNERIA E SCIENZA DELL'INFORMAZIONE

---

38123 Povo – Trento (Italy), Via Sommarive 14  
<http://www.disi.unitn.it>

AN ADAPTIVE MULTI-SCALING IMAGING TECHNIQUE BASED  
ON A FUZZY-LOGIC STRATEGY FOR DEALING WITH THE  
UNCERTAINTY OF NOISY SCATTERING DATA

M. Benedetti, A. Casagrande, M. Donelli, and A. Massa

January 2011

Technical Report # DISI-11-062



# An Adaptive Multi-Scaling Imaging Technique based on a Fuzzy-Logic Strategy for dealing with the Uncertainty of Noisy Scattering Data

Manuel Benedetti, Aronne Casagrande, Massimo Donelli, and Andrea Massa

Department of Information and Communication Technologies,  
University of Trento, Via Sommarive 14, I-38050 Trento - Italy  
Tel. +39 0461 882057, Fax +39 0461 882093

E-mail: *andrea.massa@ing.unitn.it*,

*{manuel.benedetti, aronne.casagrande, massimo.donelli}@dit.unitn.it*

Web-page: *http://www.eledia.ing.unitn.it*

# An Adaptive Multi-Scaling Imaging Technique based on a Fuzzy-Logic Strategy for dealing with the Uncertainty of Noisy Scattering Data

Manuel Benedetti, Aronne Casagrande, Massimo Donelli, and Andrea Massa

## Abstract

Inverse scattering data, even though collected in a controlled-environment, are usually corrupted by electromagnetic noise, which strongly affects the effectiveness of the reconstruction techniques because of the intrinsic ill-positioning of the problem. In order to limit the effects of the noise on the retrieval procedure and to fully exploit the limited information content available from the measurements, an innovative inversion scheme based on the integration of an adaptive multi-scale procedure and a fuzzy-logic-based decision strategy is proposed. The main goal of the approach is to reduce the complexity of the problem as well as to improve the robustness of the inversion procedure allowing an accurate retrieval of the profile under test. The approach is based on an adaptive, coarse-to-fine successive representation of the unknown object obtained through a sequence of nonlinear reconstructions where suitable weighting coefficients are defined through a fuzzy logic. Key elements of the theoretical analysis are given and several numerical examples, concerned with synthetic and experimental test cases, illustrate the consequences of the proposed approach in terms of both resolution accuracy and robustness as well as computational costs.

## Key-words:

Microwave Imaging, Inverse Scattering, Fuzzy-Logic, Iterative Multi-Scaling Approach.

# 1 Introduction

Imaging an unknown object from the field scattered by the same object when probed by an electromagnetic source is a very interesting and challenging topic [1]. Let us consider the wide range of possible applications from subsurface imaging [2] to biomedical and diagnostic applications [3]. However, several theoretical difficulties occur in developing a practical imaging system based on inverse scattering phenomena [4]. As a matter of fact, inverse scattering problems are intrinsically ill-posed and their numerical counterpart ill-conditioned because of the limited amount of information collectable from scattering experiments [5][6]. To limit/overcome these drawbacks several approaches have been proposed. Two main paths of research seem to be usually taken into account:

- Some methods, taking into account the achievable spatial resolution in relation to the amount of data [7] and the nonlinearity of the problem in hand, define suitable representations of the unknowns in order to allow reliable reconstructions through effective optimization methods both deterministic [8] and stochastic [9][10];
- Other approaches consider multi-resolution strategies in order to enhance the achievable resolution accuracy fully exploiting all the scattering information [7][11]-[13].

Nevertheless, such techniques do not consider or partially address the problem of the reliability/uncertainty of the data. As a matter of fact, if quantifying the number of informative (i.e., independent) data [6] is a key-issue in solving inverse scattering problems, on the other hand the effectiveness of a retrieval procedure strongly depends on the level of reliability of such data.

In collecting the electromagnetic measurements, experimental and environmental noises add to the scattered signals because of the mechanical positioning of the electromagnetic field sensors or the electromagnetic interferences in the test-site. The presence of these corrupting factors, because of the high intrinsic instability caused by the ill-posedness of inverse scattering problems, strongly affects the accuracy of the reconstruction without proper countermeasures.

Certainly, a direct estimation of the uncertainty/reliability associated with scattering measurements would be really useful. But, because of the cost and the complexity of such an estimate, it is quite hard to be obtained (e.g., multiplexing and time averaging of multiple measurements could be a solution strategy [14][15][16], but notwithstanding an *a-priori* knowledge on the noise type is needed). Moreover, such a knowledge usually is available not as an *objective knowledge* (i.e., in terms of a mathematical model or numerical values), but as a *subjective knowledge* (e.g., “data are affected by low noise” or “data are affected by much noise” or “data are quite reliable”), which represents an information that is usually difficult or complex (and expensive) to quantify using traditional mathematics or experimental methods. Because of these problems, subjective information is usually ignored or partially taken into account. In general, the impact of corrupted data because of the ill-posedness of the inverse problem is handled by looking for a regularized solution, which better fits all the available data (corrupted or not by the noise and characterized by a different degree of reliability) by minimizing the discrepancy function composed by two terms, namely the *Data term* and the *State term*. These terms depend on the scattered field collected in the observation domain and on the incident field measured in the investigation domain, respectively. Suitable weighting parameters heuristically defined [17][10] or iteratively tuned [18] allow one to weight more the one or the other term, depending on the uncertainties associated with both of them. In such a way, these techniques allow a “*global*” control on the whole set of data and they do not consider each measure individually with its degree of reliability. Moreover, the arising control is “*indirect*” since it does not quantify the reliability of the scattering data, but their impact on the cost function.

As far as the use of the subjective information for effectively exploiting the “clean” information (i.e., without noise and independent) contained in noisy scattering data is concerned, the following considerations should be taken into account. If the amplitude of the total field scattered by the target under test is small, then the collected samples might be easily and irremediably affected by e.m. experimental and environmental noises. On the contrary, the higher is the amplitude of the field samples, the lower is the risk of being heavily corrupted. Starting from these physical bases, this paper proposes an innovative

automatic approach preliminary assessed in [19] and here integrated with a customized iterative multi-scaling procedure, which takes into account the uncertainty on the reliability of the measured data, due to the presence of the noise, through a fuzzy-logic-based strategy [20]. To the best of the authors' knowledge, although fuzzy theory has been widely employed especially in the framework of automated controls [21][22] where uncertainty and *subjective knowledge* play an important role, its use in the framework of electromagnetics has been limited for example to the fuzzy partitioning of ANNs input space [23], to the combination of competing objective functions [24], and to determine the values of regularization parameters in ECT applications [25]. Therefore, in the authors' opinion, the use of a fuzzy-based strategy for dealing with the uncertainty on the reliability of noisy scattered data represents a novelty in the framework of microwave imaging.

The underlying idea of the proposed approach is that of defining a system able to react automatically to any noisy condition providing a degree of reliability of the scattering data so that they can be usefully employed during the retrieval process and for an "amount" related to their accuracy [i.e., by properly weighting the required fitting between each sample of measured and reconstructed data, see Eq. (6)]. The system is required to give such an indication starting from the same measured data without other *a-priori* information or constraints both on scatterers and on the acquisition setup.

The paper is structured as follows. A brief description of a standard two-dimensional microwave imaging problem will be given in Sect. 2 where a suitable weighted multi-resolution cost function will be defined in order to conveniently take into account the presence of corrupted scattering data fully exploiting the available information content. Then, a detailed explanation of the fuzzy-logic-based strategy and of its customization to the microwave imaging framework will be presented in Sect. 3. Sect. 4 will be devoted to the calibration and numerical testing of the fuzzy logic system (*FLS*). The criterion for selecting the *FLS* descriptive parameters will be briefly summarized and the results of a sensitive analysis will be discussed in order to define the optimal setting (Sub-Sect. 4.1). In Sub-Sect. 4.2, a numerical assessment will be performed by considering different scattering scenarios (synthetic as well as experimental) and various environmental conditions. Moreover, a comparative study among the proposed approach and the standard

*IMSA* as well as with state-of-the-art regularization methods will be carried out. Finally some conclusions will be drawn and future developments will be proposed (Sect. 5).

## 2 Inverse Problem Formulation

Let us consider a cylindrical two-dimensional geometry where a set of  $V$  transverse-magnetic (*TM*) plane waves  $\mathbf{E}_{inc}^v(x, y) = E_{inc}^v(x, y) \hat{\mathbf{z}}$ ,  $v = 1, \dots, V$ , successively illuminates an investigation domain denoted by  $\Gamma_{inv}$  where an unknown inhomogeneous dielectric object is supposed to lie. Without loss of generality, the host medium is a homogeneous, non-magnetic and lossless background with dielectric properties equal to that of the vacuum ( $\varepsilon_0, \mu_0$ ). The dielectric inhomogeneity that identifies the unknown scatterer is described by means of the distribution of the object function  $\tau$  given by

$$\tau(x, y) = [\varepsilon_R(x, y) - 1] - j \frac{\sigma_c(x, y)}{2\pi f \varepsilon_0} \quad (1)$$

where  $\varepsilon_R$  and  $\sigma_c$  are the relative dielectric permittivity and the electric conductivity of the scatterer, respectively, and  $f$  is the working frequency of the probing source.

The field scattered by the scenario under test  $\mathbf{E}_{scatt}^v(x, y) = E_{scatt}^v(x, y) \hat{\mathbf{z}}$ ,  $v = 1, \dots, V$ , is collected in an external observation domain  $\Gamma_{obs}$  where a set of  $M(v)$ ,  $v = 1, \dots, V$ , measurement points are uniformly distributed. Starting from the knowledge of the scattered field and of the incident field radiated by the electromagnetic source, the scatterer is usually reconstructed/imagined by solving the nonlinear inverse scattering equations:

$$\begin{aligned} E_{scatt}^v(x_{m(v)}, y_{m(v)}) &= k_0^2 \int_{\Gamma_{inv}} G_{2D}(x_{m(v)}, y_{m(v)} | x', y') \tau(x', y') E_{tot}^v(x', y') dx' dy' \\ (x_{m(v)}, y_{m(v)}) &\in \Gamma_{obs} \quad m(v) = 1, \dots, M(v), \quad v = 1, \dots, V \end{aligned} \quad (2)$$

$$\begin{aligned} E_{inc}^v(x, y) &= E_{tot}^v(x, y) - k_0^2 \int_{\Gamma_{inv}} G_{2D}(x, y | x', y') \tau(x', y') E_{tot}^v(x', y') dx' dy' \\ (x, y) &\in \Gamma_{inv} \quad v = 1, \dots, V \end{aligned} \quad (3)$$

where  $G_{2D}$  denotes the Green function of the background medium and  $E_{tot}^v$  is the field with the object. Towards this end, since a closed-form solution is generally not available,

a suitable discretization is performed for allowing a numerical solution. As far as the well-known Richmond's procedure [26] is concerned, the investigation domain is equally partitioned into  $N$  sub-domains of area  $A_n$ ,  $n = 1, \dots, N$ .

However, because of the limited information content available from scattering data [6], multi-resolution strategies are necessary [11]-[12] for achieving a suitable resolution of the object function in  $\Gamma_{inv}$  keeping a limited number of unknowns at the same time. In such a framework, the iterative multi-scaling approach [13] can be profitably used. By assuming a multi-resolution representation of the problems unknowns, namely the object function

$$\tau(x, y) = \sum_{r=1}^{R(s)} \sum_{n(r)=1}^{N(r)} \tau(x_{n(r)}, y_{n(r)}) B_{n(r)}(x, y) \quad (x, y) \in \Gamma_{inv} \quad (4)$$

and of the total field

$$E_{tot}^v(x, y) = \sum_{r=1}^{R(s)} \sum_{n(r)=1}^{N(r)} E_{tot}^v(x_{n(r)}, y_{n(r)}) B_{n(r)}(x, y) \quad (x, y) \in \Gamma_{inv} \quad (5)$$

where  $r$  is the resolution index at the  $s$ -th step of multi-scaling process,  $n(r)$  denotes the corresponding discretization sub-domain in  $D_{inv}$ , and  $B_{n(r)}$  is a known rectangular basis function defined over the  $n(r)$ -th sub-domain, the *IMSA* consists of a sequence of  $S$  successive reconstructions ( $s = 1, \dots, S$ ) of the unknown coefficients coded into the array  $\underline{f}^{(s)} = \{\tau(x_{n(r)}, y_{n(r)}), E_{tot}^v(x_{n(r)}, y_{n(r)}); n(r) = 1, \dots, N(r); r = 1, \dots, R(s)\}$ ,  $R(s) = s$  being the current resolution index. Towards this end and at each step  $s$ , the following multi-resolution cost function is minimized

$$\begin{aligned} \Phi_{IMSA}^{(s)} \left\{ \underline{f}^{(s)} \right\} &= \frac{\sum_{v=1}^V \sum_{m(v)=1}^{M(v)} \left| E_{scatt}^v(x_{m(v)}, y_{m(v)}) - \Phi_{Data} \left\{ \underline{f}^{(s)} \right\} \right|^2}{\sum_{v=1}^V \sum_{m(v)=1}^{M(v)} \left| E_{scatt}^v(x_{m(v)}, y_{m(v)}) \right|^2} \\ &+ \frac{\sum_{v=1}^V \sum_{r=1}^{R(s)} \sum_{n(r)=1}^{N(r)} w(x_{n(r)}, y_{n(r)}) \left| E_{inc}^v(x_{n(r)}, y_{n(r)}) - \Phi_{State} \left\{ \underline{f}^{(s)} \right\} \right|^2}{\sum_{v=1}^V \sum_{r=1}^{R(s)} \sum_{n(r)=1}^{N(r)} \left| w(x_{n(r)}, y_{n(r)}) E_{inc}^v(x_{n(r)}, y_{n(r)}) \right|^2} \end{aligned} \quad (6)$$

where the first term represents the normalized global mismatch between estimated (from

the reconstruction of  $\underline{f}^{(s)}$ )

$$\Phi_{Data} \left\{ \underline{f}^{(s)} \right\} = \sum_{r=1}^{R(s)} \sum_{n(r)=1}^{N(r)} w(x_{n(r)}, y_{n(r)}) \tau(x_{n(r)}, y_{n(r)}) E_{tot}^v(x_{n(r)}, y_{n(r)}) G_{2D}(k_0 \rho_{m(v)n(r)}) \quad (7)$$

and measured data in  $\Gamma_{obs}$  [i.e.,  $E_{scatt}^v(x_{m(v)}, y_{m(v)})$ ], while the second term is the normalized global error in matching the *State Equation* since

$$\Phi_{State} \left\{ \underline{f}^{(s)} \right\} = E_{tot}^v(x_{n(r)}, y_{n(r)}) - \sum_{p(r)=1}^{N(r)} \tau(x_{p(r)}, y_{p(r)}) E_{tot}^v(x_{p(r)}, y_{p(r)}) G_{2D}(k_0 \rho_{n(r)p(r)}) \quad (8)$$

determines the estimated value of the incident field in  $\Gamma_{inv}$ .

Moreover,  $w$  is a weighting function

$$w(x_{n(r)}, y_{n(r)}) = \begin{cases} 0 & \text{if } (x_{n(r)}, y_{n(r)}) \notin D^{(s-1)} \\ 1 & \text{if } (x_{n(r)}, y_{n(r)}) \in D^{(s-1)} \end{cases} \quad (9)$$

and  $D^{(s-1)}$  the support of the Region-of-Interest (*RoI*) where the unknown scatterer has been detected at the  $(s-1)$ -th step [13]. Starting from the coarse reconstruction achieved at the first step ( $s=1$ ,  $D^{(s-1)} = \Gamma_{inv}$ ), the iterative “*zooming*” process is repeated until the “*stationary*” condition [13] holds true ( $s = S_{opt}$ ).

Although such a formulation allows an effective use of the available scattering data in terms of the achievable spatial resolution, it does not take into account the uncertainty on the reliability of the scattering data [ $E_{scatt}^v(x_{m(v)}, y_{m(v)})$  and  $E_{inc}^v(x_{n(r)}, y_{n(r)})$ ], which in real applications are usually corrupted by equivalent sources of noise.

In order to fully exploit the available subjective knowledge on the scattering data and to take into account the uncertainty/reliability associated with the measurements, let us represent/quantify the uncertainty/reliability-degree of the data by introducing in (6) a set of suitable weighting parameters  $\alpha_{m(v)}$  and  $\beta_{n(r),v}$ . Thus, the arising *IMSA – Fuzzy* cost function is expressed as follows

$$\begin{aligned}
\Phi_{IMSA-Fuzzy}^{(s)} \{ \underline{f}^{(s)} \} &= \frac{\sum_{v=1}^V \sum_{m(v)=1}^{M(v)} \left\{ \alpha_{m(v)} \left| E_{scatt}^v (x_{m(v)}, y_{m(v)}) - \Phi_{Data} \{ \underline{f}^{(s)} \} \right|^2 \right\}}{\sum_{v=1}^V \sum_{m(v)=1}^{M(v)} \left| E_{scatt}^v (x_{m(v)}, y_{m(v)}) \right|^2} \\
&+ \frac{\sum_{v=1}^V \sum_{r=1}^{R(s)} \sum_{n(r)=1}^{N(r)} \left\{ \beta_{n(r),v} w (x_{n(r)}, y_{n(r)}) \left| E_{inc}^v (x_{n(r)}, y_{n(r)}) - \Phi_{State} \{ \underline{f}^{(s)} \} \right|^2 \right\}}{\sum_{v=1}^V \sum_{r=1}^{R(s)} \sum_{n(r)=1}^{N(r)} \left| w (x_{n(r)}, y_{n(r)}) E_{inc}^v (x_{n(r)}, y_{n(r)}) \right|^2}
\end{aligned} \tag{10}$$

where the weighting parameters are computed starting from a fuzzy representation of the uncertainty associated with the measurements and by means of a fuzzy logic based strategy described in the following section (Sect. 3).

### 3 The Fuzzy-Logic Strategy

The framework of fuzzy logic (*FL*) is unique in its ability to represent subjective or linguistic knowledge in terms of a mathematical model. Furthermore, its coupling with rule-based systems is enabling the modeling of the approximate and imprecise reasoning processes common in human problem solving [21]. Therefore, *FLS*s have been widely used in the last decades especially in the field of automatic controls after Zadeh introduced the basic principles of *FL* and approximate reasoning in his pioneering work [20]. For an overview, the interested reader is suggested to refer to the dated and classical references on *FL* and systems. For example, [27][28] as well as [29][30][31][32] and the references cited therein.

Generally speaking, a *FLS* system can be described through the block-diagram in Fig. 1(a). The *FLS* maps a crisp input (or a collection of crisp inputs) into a crisp output. At the heart of the *FLS* Fig. 1 [Fig. 1(a)] there is a fuzzy rule base, which contains fuzzy rules expressed in the form of *IF – THEN* statements. The mapping of the input data to the desired output is generally performed in three stages. These are the *fuzzification* of the input data (assuming this data is crisp), the *fuzzy inference* using fuzzy rules, and a *defuzzification* stage used for producing a crisp scalar output. Usually, if the rule base of the *FLS* includes several rules, their individual outputs are combined in the inference stage for producing a single fuzzy output set.

### 3.1 The *FLS* for Electromagnetic Imaging

Let us refer to the block diagram shown in Fig. 1(b). The proposed implementation of a fuzzy-logic strategy for automatically evaluating the level of uncertainty on the reliability of measured data needs of a normalization step before the fuzzy-logic system. The *normalization block*, characterized by the transfer function  $N\{\cdot\}$ , defines the crisp inputs to the fuzzy system starting from the knowledge of the total and scattered electric field in the observation domain and of the incident electric field in the investigation domain. Such normalized values are computed as follows

$$\eta_{m(v)} = N \left\{ E_{scatt}^v(x_{m(v)}, y_{m(v)}), E_{tot}^v(x_{m(v)}, y_{m(v)}) \right\} = \frac{\left| \frac{E_{scatt}^v(x_{m(v)}, y_{m(v)})}{E_{tot}^v(x_{m(v)}, y_{m(v)})} \right|}{\max_v \left\{ \max_{m(v)} \left| \frac{E_{scatt}^v(x_{m(v)}, y_{m(v)})}{E_{tot}^v(x_{m(v)}, y_{m(v)})} \right| \right\}} \quad (11)$$

$$\xi_{n(r),v} = N \left\{ E_{inc}^v(x_{n(r)}, y_{n(r)}) \right\} = \frac{\left| E_{inc}^v(x_{n(r)}, y_{n(r)}) \right|}{\max_v \left\{ \max_r \left[ \max_{n(r)} \left| E_{inc}^v(x_{n(r)}, y_{n(r)}) \right| \right] \right\}} \quad (12)$$

in order to “rank” the whole set of scattering data in terms of their relative amplitudes according to the idea that the higher is the normalized amplitude of a sample, the lower is its risk of being heavily corrupted as well as the uncertainty on its reliability for reconstruction purposes. Then, in order to obtain a reliability index for each measurement, the normalized coefficients  $\eta_{m(v)}$  and  $\xi_{n(r),v}$  are mapped into the crisp coefficients  $\alpha_{m(v)}$  and  $\beta_{n(r),v}$  by means of the transfer function  $\mathfrak{F}\{\cdot\}$  schematically-described in the block diagram shown in Fig. 1(a). More in detail, given a set of rules ( $\mathfrak{R}_i, i = 1, \dots, I, I$  being the number of rules) defined by a set of antecedents/premises ( $A_i, i = 1, \dots, I$ ) and relative consequences/conclusions ( $C_i, i = 1, \dots, I$ ), the inference process proceeds in five steps.

1. **Inputs Fuzzification** - The *fuzzifier*  $\Omega\{\cdot\}$  applies to the actual values of the coefficients  $\eta_{m(v)}$  and  $\xi_{n(r),v}$  the *Gaussian membership function*  $\mu(\cdot)$  in order to determine the degree to which they belong to the appropriate fuzzy sets  $F_i$  defined in each premise  $A_i$ . The Gaussian function is defined as

$$\mu(\eta; \eta_{m(v)}; \sigma) = \frac{1}{\sqrt{2\pi\sigma^2}} \exp\left(-\frac{(\eta - \eta_{m(v)})^2}{\sigma^2}\right) \quad (13)$$

or

$$\mu(\xi; \xi_{n(r),v}; \sigma) = \frac{1}{\sqrt{2\pi\sigma^2}} \exp\left(-\frac{(\xi - \xi_{n(r),v})^2}{\sigma^2}\right) \quad (14)$$

centered in correspondence with the actual value of the input coefficient ( $\eta_{m(v)}$  or  $\xi_{n(r),v}$ ) and characterized by a variance value  $\sigma$  proportional to the uncertainty level associated to the current measure;

2. **Rule Activation** - Once the crisp input has been fuzzified, the  $i$ -th rule  $\mathfrak{R}_i$  is activated when there is a non-zero degree of similarity between the fuzzy input [ $\mu(\eta; \eta_{m(v)}; \sigma)$  or  $\mu(\xi; \xi_{n(r),v}; \sigma)$ ] and the antecedent  $A_i$ . Mathematically, it can be expressed as follows

$$\mu(\eta; \eta_{m(v)}; \sigma) \cap A_i(\eta) \neq \{0\} \Rightarrow \mathfrak{R}_i \text{ activated} \quad (15)$$

$$\mu(\xi; \xi_{n(r),v}; \sigma) \cap A_i(\xi) \neq \{0\} \Rightarrow \mathfrak{R}_i \text{ activated.} \quad (16)$$

The activation value of each rule,  $R_i$ , is computed evaluating the highest value among the intersection points between the membership function of the  $i$ -th antecedent  $A_i$  and the membership function associated to the input. Analytically,

$$R_i = \max_{\eta \in [0,1]} \{\mu(\eta) : \mu(\eta; \eta_{m(v)}; \sigma) = A_i(\eta)\} \quad (17)$$

$$R_i = \max_{\xi \in [0,1]} \{\mu(\xi) : \mu(\xi; \xi_{n(r),v}; \sigma) = A_i(\xi)\}; \quad (18)$$

3. **Rule Implication** - The output fuzzy subset  $G'_i$ , to be assigned to each output variable of each rule, is computed by defining the corresponding membership function [ $C'_i(\alpha)$  or  $C'_i(\beta)$ ] through the *MIN* inferencing rule [33] starting from the activation value  $R_i$ . The output membership function  $C_i$  (defining the fuzzy set  $G_i$ ) is clipped off at a height corresponding to the degree of truth  $R_i$  of the premise  $A_i$

$$C'_i(\alpha) = \min_{\alpha \in [0,1]} \{C_i(\alpha), R_i\}, \quad \alpha \in [0, 1] \quad (19)$$

$$C'_i(\beta) = \min_{\beta \in [0,1]} \{C_i(\beta), R_i\}, \quad \beta \in [0, 1]; \quad (20)$$

4. **Output Fuzzy Subsets Aggregation** - Since decisions are based on the testing of the whole set of rules  $\{\mathfrak{R}_i, i = 1, \dots, I\}$ , the rules must be combined in order to make a decision. The list of truncated output fuzzy sets  $\{G'_i, i = 1, \dots, I\}$  returned by the implication process for each rule are combined (“*aggregation*” process) into a single output fuzzy set  $O$ . The membership function  $\vartheta$  of the aggregate output fuzzy set  $O$  is computed taking the maximum value among all the output membership functions  $\{C'_i, i = 1, \dots, I\}$

$$\vartheta(\alpha) = \max_{i=1, \dots, I} \{C'_i(\alpha)\}, \quad \alpha \in [0, 1] \quad (21)$$

$$\vartheta(\beta) = \max_{i=1, \dots, I} \{C'_i(\beta)\}, \quad \beta \in [0, 1]; \quad (22)$$

5. **Defuzzification** - The defuzzification block  $\Theta\{\cdot\}$  is used for converting the aggregate fuzzy output set  $O$  into the reliability coefficient  $\alpha_{m(v)}$  (or  $\beta_{n(r),v}$ ) concerned with the normalized coefficient  $\eta_{m(v)}$  (or  $\xi_{n(r),v}$ ), respectively. For its simplicity, let us consider the so-called *height defuzzifier* [34]. Let  $\bar{g}_i$  denote the center of gravity of the fuzzy set  $G_i$ , then the defuzzifier computes the cost function weighting coefficients as follows

$$\alpha_{m(v)} = \frac{\sum_{i=1}^I [\bar{g}_i C'_i(\alpha = \bar{g}_i)]}{\sum_{i=1}^I C'_i(\alpha = \bar{g}_i)} \quad (23)$$

$$\beta_{n(r),v} = \frac{\sum_{i=1}^I [\bar{g}_i C'_i(\beta = \bar{g}_i)]}{\sum_{i=1}^I C'_i(\beta = \bar{g}_i)}. \quad (24)$$

## 4 Numerical Analysis and Testing

The aim of this section is twofold. Firstly, a sensitivity analysis on the impact of some *FLS* parameters on the reconstruction performance are reported to determine their optimal

setting for microwave imaging. Then, by considering such an optimal configuration, the effectiveness and robustness of the *FL*-based approach are assessed in reconstructing different scattering scenarios starting from synthetically-generated as well as experimental inverse scattering data.

#### 4.1 *FLS* Calibration

Several choices could be made in defining each block of the diagram of the *FLS* shown in Fig. 1(a). As a matter of fact, the *FLS* user is requested to decide on the type of fuzzification (singleton or non-singleton), mathematical expression of the membership functions (triangular, trapezoidal, Gaussian, etc...), descriptive parameters of the membership functions, implication (*MIN* inference or *PRODUCT* inference rule), aggregation rule (*MAX* or *SUM*), and defuzzifier (maximum, mean-of-maxima, centroid, height, etc...).

In our implementation, a *non-singleton fuzzifier* has been selected for the fuzzification procedure. Unlike the *singleton fuzzifier*, such a fuzzifier is characterized by a Gaussian membership function  $\mu(\varsigma; \bar{\varsigma}; \sigma)$  (centered in  $\bar{\varsigma}$  and with variance  $\sigma$ ) in order to take into account the uncertainty concerned with the reliability of measured data [33]. Concerning the other choices for the inference block, because of our interest in the engineering application of *FL*, the criterion of the *computational simplicity* has been adopted. Therefore, triangular/trapezoidal membership functions  $\{C_i, i = 1, \dots, I\}$  have been used by representing linguistic variables (e.g., *reliability of measured data*, *amplitude*  $\in \{\textit{slight}, \textit{low}, \textit{medium}, \textit{strong}, \textit{high}\}$ ) in terms of fuzzy sets [33]-[37]. Moreover, simple inference rules (*MIN* inference and *MAX* composition) have been considered in the implication and aggregation phase, respectively. Furthermore, the *height defuzzifier* has been adopted for simplicity since the centers of gravity  $\{\bar{g}_i, i = 1, \dots, I\}$  of triangular/trapezoidal membership functions are *a-priori* known.

Nevertheless these assumptions/simplifications, the *FLS* needs of a careful tuning of the remaining parameters, which are expected to affect the imaging performances. Therefore, a sensitivity study on the effects of the parameter  $\sigma$  of the *non-singleton Gaussian fuzzifier* and of the fuzzy rules has been performed for presenting a reliable *FL*-based approach for

microwave imaging. Towards this end, the following experiments have been carried out:

- *Experiment 1* - Different sets of rules, defined according to the suggestions in the reference literature, have been analyzed;
- *Experiment 2* - The value of  $\sigma$  has been varied in a range of admissible values,  $\sigma \in [10^{-5}, 10^{-1}]$ , for attributing the more appropriate level of uncertainty to the scattering data.

As a measure of effectiveness, the values of the quantitative error indexes ( $\zeta_{tot}$  = total reconstruction error,  $\zeta_{int}$  = internal reconstruction error, and  $\zeta_{ext}$  = external reconstruction error) defined in [13] have been used and the following reference scenarios have been considered:

- *Scenario 1* - A square homogeneous investigation domain  $\Gamma_{inv}$ ,  $L_{inv} = 1.125 \lambda_0$ -sided, where an off-centered dielectric homogeneous scatterer of side  $l = 0.2 \lambda_0$  and object function  $\tau = 1.5$  is located at  $x_c = y_c = 0.3 \lambda_0$ . Moreover, a multi-illumination/multi-view imaging setup characterized by  $V = 4$  views and  $M(v) = 20$ ,  $v = 1, \dots, V$  equally-spaced sensors on a circular domain  $\Gamma_{obs}$  (of radius  $r_{obs} = 1.125 \lambda_0$ ) has been used for probing the scattering configuration under test.;
- *Scenario 2* - A square homogeneous dielectric ( $\tau = 1.5$ ) cylinder of side  $l = 1.2 \lambda_0$  located in a  $L_{inv} = 4 \lambda_0$ -sided investigation domain at  $x_c = 0.4 \lambda_0$  and  $y_c = 1.0 \lambda_0$ .  $\Gamma_{inv}$  has been illuminated by  $V = 8$  plane waves and the scattering data have been collected in  $M(v) = 50$ ,  $v = 1, \dots, V$  measurement points on a circular observation domain  $\Gamma_{obs}$  with radius  $r_{obs} = 2.93 \lambda_0$ .

In order to simulate noisy conditions, the scattering data have been corrupted by adding a synthetic Gaussian noise characterized by an assigned signal-to-noise ratio ( $SNR$ ) [13]. Consequently, in order to take into account the stochastic nature of the noise, each test case has been repeated  $P = 100$  times with the same parameters setup and the average

values of the error indexes

$$\bar{\zeta}_j = \frac{1}{P} \sum_{p=1}^P \zeta_j \quad j = tot, int, ext \quad (25)$$

have been recorded.

Furthermore, because of the needs of focusing on *FLS* by evaluating the effects of its characteristic parameters, “bare” reconstructions (i.e., single-step homogeneous-resolution inversions) have been carried out neglecting the “overboost” effect of the multi-step procedure. Accordingly,  $\Gamma_{inv}$  has been uniformly-partitioned into  $N = 15 \times 15$  (*Scenario 1*) and  $N = 45 \times 45$  (*Scenario 2*) square sub-domains.

#### 4.1.1 Experiment #1

As a general criterion for defining the set of rules, let us consider that a greater resolution is generally achieved by using more membership functions at the price of greater computational complexity. Moreover, membership functions can be made to overlap in order to distribute our decision on the data reliability over more than one input class making the *FLS* more robust. Concerning the definition of customized rules for the imaging problem, the following key-points have been taken into account: (i) the smallest is the amplitude of the measured field, more relevant could be the blurring/masking effect of the noise; (ii) the greater is the amplitude of the field scattered by the object (i.e.,  $E_{tot}^v$ ) compared to the incident field (i.e.,  $E_{scatt}^v$  - where a sort of “print” of the scatterer is “coded” - is not negligible), the higher is usually the information on the scatterer collectable from scattering data.

Starting from these considerations and from known reference configurations, the sets of rules pictorially-represented in Fig. 2 have been deduced by interpreting, according to the guidelines in [33]-[37], the linguistic variables concerned with the amplitudes of the field samples for the antecedents, and the value of the reliability coefficient  $\alpha_{m(v)}$  (or  $\beta_{n(r),v}$ ) for the consequences. More in detail, the sets of rules (i.e., antecedents and consequences) of Figs. 2(a)-(l) have been generated by varying position and shape of their fuzzy sets. Then, the most suitable rule has been chosen by using each pair of antecedents/consequences

in reconstructing both reference scenarios and by evaluating its effectiveness in terms of inversion accuracy. Table 1 summarizes the obtained results in a representative situation when  $SNR = 5\text{ dB}$  [Tab. I (a) - *Scenario 1* and Tab. I (b) - *Scenario 2*]. As it can be noticed, the smallest values of the error indexes occur in correspondence with the set of rules #3. Such a situation usually verifies whatever the  $SNR$  value.

#### 4.1.2 Experiment #2

Under the assumption of a *non-singleton Gaussian fuzzifier*, the level of uncertainty on inputs depends on the variance  $\sigma$ . Let us consider that the higher is the  $\sigma$  value, the greater is the uncertainty of data. Otherwise, when the reliability of the measures is high, then  $\sigma$  reduces to 0 and the Gaussian membership function becomes of singleton type. However, no analytical rules for defining the optimal variance value exist (to the best of the authors' knowledge), thus a heuristic calibration must be carried out. Towards this end,  $\sigma$  has been varied in the range between  $10^{-5}$  and  $10^{-1}$  by considering various noisy conditions (i.e., different  $SNR$  values). Since the positive effect of the *FL*-based strategy is expected to occur when significant levels of noise are present, the situation characterized by a  $SNR = 5\text{ dB}$  has been assumed as a representative test case. Fig. 3 illustrates the behavior of the *FLS* in terms of averaged error figures when dealing with *Scenario 1*. Although non-so-significant differences arise, the value of  $\sigma = 10^{-4}$  guarantees the best reconstruction providing the smallest values of the error figures ( $\bar{\zeta}_{tot} = 6.38$ ,  $\bar{\zeta}_{int} = 23.10$ , and  $\bar{\zeta}_{ext} = 5.68$ ). The same considerations hold true for the *Scenario 2*, as well.

In conclusion, the following parametric configuration will be our reference *FLS* setup: set of rules #3 and  $\sigma = 10^{-4}$ .

## 4.2 Testing

In this section, the potentialities of the proposed *FL*-based microwave imaging technique will be assessed by presenting a selected set of results from several numerical experiments.

The behavior of the proposed method will be illustrated by considering different scatterers and synthetic noisy conditions (Sect. 4.2.1). Moreover, the inversion of experimentally-acquired data will be dealt with for a check in a real framework (Sect. 4.2.2).

The obtained results will be mainly compared with those from the standard implementation of the *IMSA* [13] in order to show the enhancement in the reconstruction accuracy allowed by the *FL* strategy when dealing with noisy/corrupted data. As far as the *IMSA* is concerned, the *RoI* has been partitioned into  $N(R) = 10 \times 10$  square sub-domains. Moreover, the minimization of (10) has been iteratively performed with a deterministic conjugate-gradient procedure [13] with a maximum number of iterations at each step fixed to  $K^{(s)} = 2000$ ,  $s = 1, \dots, S_{opt}$ . The use of a deterministic technique for this analysis is motivated by the need of focusing on the improvement guaranteed by the use of a *FLS* neglecting the randomness arising from the integration of the reconstruction procedure with a stochastic optimizer (more effective in avoiding the solution is trapped in the local minima of the cost function).

#### 4.2.1 Numerical Assessment

The first example is aimed at showing the effect of the reliability indexes  $\alpha_{m(v)}$  and  $\beta_{n(r),v}$  on the reconstruction capabilities of the imaging procedure in different noisy conditions. The grey-scale representations<sup>(1)</sup> of the reconstructions obtained without and exploiting the *FLS* are reported in Fig. 4 for different *SNR* values when the so-called *Scenario 2* is taken into account. As requested in defining the guidelines of the *FLS*, when the noise level is non-so-significant ( $SNR \geq 20$  dB), the *FL* block behaves in a “transparent” way and its effect in terms of reconstruction accuracy appears almost negligible as pictorially shown in Figs. 4(a) and 4(b) and quantitatively confirmed by the averaged values of the error figures in Tab. II ( $\bar{\zeta}_{tot}]_{IMSA} = 5.98$  vs.  $\bar{\zeta}_{tot}]_{IMSA-Fuzzy} = 5.45$ ,  $\bar{\zeta}_{ext}]_{IMSA} = 5.77$  vs.  $\bar{\zeta}_{ext}]_{IMSA-Fuzzy} = 5.16$ , and  $\bar{\zeta}_{int}]_{IMSA} = 11.78$  vs.  $\bar{\zeta}_{tot}]_{IMSA-Fuzzy} = 10.40$ ).

On the other hand and as expected, the fuzzy data processing, which acts before the cost function minimization, significantly impacts when  $SNR < 20$  dB, that is in those

---

<sup>(1)</sup> The actual support of the scatterer is denoted by the dashed line and the black pixel in the lower right border is used for reference.

situations where the measured data are seriously corrupted by the noise. Such an event can be clearly observed comparing the representative samples of reconstructed profiles shown in Figs. 4(c)-(d) ( $SNR = 10\text{ dB}$ ) and Figs. 4(e)-(f) ( $SNR = 5\text{ dB}$ ). As a matter of fact, when the level of noise increases, the dielectric profile reconstructed by means of the standard *IMSA* presents some inhomogeneities [ $SNR = 10\text{ dB}$  - Fig. 4(c)] and some artifacts adds in heavy noise conditions [ $SNR = 5\text{ dB}$  - Fig. 4(e)]. Whereas, the images retrieved by the *FL*-based system are more homogeneous and quite faithfully fit the actual shape of the scatterer whatever the  $SNR$  value [Figs. 4(d)-(f)]. For comparison purposes, let us consider that on average  $\frac{\bar{\zeta}_{int}]_{IMSA}}{\bar{\zeta}_{int}]_{IMSA-Fuzzy}} \Big|_{SNR=10\text{ dB}} \simeq 1.5$  and  $\frac{\bar{\zeta}_{int}]_{IMSA}}{\bar{\zeta}_{int}]_{IMSA-Fuzzy}} \Big|_{SNR=5\text{ dB}} \simeq 1.3$ , and  $\frac{\bar{\zeta}_{ext}]_{IMSA}}{\bar{\zeta}_{ext}]_{IMSA-Fuzzy}} \Big|_{SNR=5\text{ dB}} \simeq 1.8$ .

The performances of the *IMSA-Fuzzy* and *IMSA* are summarized in Fig. 5 where the plots of both qualitative error indexes ( $\bar{\delta}$  and  $\bar{\Delta}$  defined as in [13]) and the quantitative error figures  $\bar{\zeta}_j$  ( $j = \{tot, int, ext\}$ ) versus  $SNR$  are shown. On average, the *IMSA-Fuzzy* usually overcomes the standard approach in locating as well as in shaping [Fig. 5(a)] the scatterer. Such a behavior is more and more evident as the noise level increases. As far as the localization error is concerned, we have  $\frac{\bar{\delta}]_{IMSA}}{\bar{\delta}]_{IMSA-Fuzzy}} \Big|_{SNR=15\text{ dB}} \simeq 1.5$ ,  $\frac{\bar{\delta}]_{IMSA}}{\bar{\delta}]_{IMSA-Fuzzy}} \Big|_{SNR=10\text{ dB}} \simeq 2.0$ , and  $\frac{\bar{\delta}]_{IMSA}}{\bar{\delta}]_{IMSA-Fuzzy}} \Big|_{SNR=5\text{ dB}} \simeq 3.0$ . Similarly, it happens for the area-estimation error  $\bar{\Delta}$ :  $\frac{\bar{\Delta}]_{IMSA}}{\bar{\Delta}]_{IMSA-Fuzzy}} \Big|_{SNR=15\text{ dB}} \simeq 1.2$ ,  $\frac{\bar{\Delta}]_{IMSA}}{\bar{\Delta}]_{IMSA-Fuzzy}} \Big|_{SNR=10\text{ dB}} \simeq 2.0$ , and  $\frac{\bar{\Delta}]_{IMSA}}{\bar{\Delta}]_{IMSA-Fuzzy}} \Big|_{SNR=5\text{ dB}} \simeq 2.7$ . On the other hand, Fig. 5(b) further points out the positive effect of the *FL*-based strategy in the faithful reconstruction of the dielectric distribution of the scatterer since on average  $\frac{av_{SNR}\{\bar{\zeta}_{int}]_{IMSA}\}}{av_{SNR}\{\bar{\zeta}_{int}]_{IMSA-Fuzzy}\}} \simeq 1.7$ .

For comparison purposes, let us consider the inversion results of the same configuration by using, for example, two regularization methods, namely the Tikhonov [38] [Figs. 6(a), (c), and (e)] and the Landweber [5] [Figs. 6(b), (d), and (f)] methods. Whatever the noise level, the actual square cylinder is neither localized nor shaped. On the other hand, since the condition of “*weak scatterer*” does not hold true, also the Born approach (even though in noiseless conditions) is not able at achieving a satisfactory reconstruction [Fig. 6(g)].

From the computational point of view, the *IMSA-Fuzzy* technique favorably compares with the standard multi-resolution approach and the minimization of the *IMSA* cost function benefits of the action of the reliability coefficients  $\alpha_{m(v)}$  and  $\beta_{n(r),v}$  as pointed out in Fig. 7 where some representative samples of the cost function versus the iteration number  $k$  are shown [Fig. 7(a) -  $SNR = 20 dB$ , Fig. 7(b) -  $SNR = 10 dB$ , and Fig. 7(c) -  $SNR = 5 dB$ ]. As it can be observed, the total number of iterations needed for achieving the stationary condition defined as  $K_{opt} = \sum_{s=1}^{S_{opt}} k_{conv}^{(s)}$  ( $k_{conv}^{(s)}$  being the number of iterations needed to achieve “convergence” at the  $s$ -th step of the multi-scaling process,  $k_{conv}^{(s)} \leq K^{(s)}$ ) usually increases when the noise level grows and the *IMSA* is used, while it keeps an almost constant value ( $K_{opt} \simeq 1200$ ) when the *FL*-based strategy is adopted. In order to numerically analyze the convergence issue, let us consider the behavior of the convergence index  $\Delta K_{opt}$  defined as follows

$$\Delta K_{opt} = \frac{\{K_{opt}\}_{IMSA} - \{K_{opt}\}_{IMSA-Fuzzy}}{\{K_{opt}\}_{IMSA}} \times 100 \quad (26)$$

for different noisy conditions (Fig. 8). As expected, because of the positive effect of the *FLS* in dealing with corrupted scattering data, the value of  $\Delta K_{tot}$  grows as the  $SNR$  value decreases. Moreover, in correspondence with low levels of noise ( $SNR > 30 dB$ ), the computational performances of the two approaches are very similar further confirming the “transparent” behavior of the *FLS* in these conditions. Therefore, the proposed approach allows a saving of the total number of iterations especially dealing with noisy data. Such a reduction guarantees a computational saving greater than the computational load due to the use of the *FLS* since the coefficients  $\alpha_{m(v)}$  and  $\beta_{n(r),v}$  are computed once and off-line. The second experiment is aimed at evaluating the dependence of the reconstruction capability of the proposed *FL*-based approach on the dimension of the object under test. Towards this purpose, the side of the homogeneous ( $\tau = 1.5$ ) square cylinder has been varied from  $l = 0.24 \lambda_0$  up to  $l = 0.72 \lambda_0$  and a noise characterized by  $SNR = 5 dB$  has been added to scattering data. Although the values of the error indexes increase as the support of the actual scatterer enlarges (Fig. 9), it should be noticed that the dynamics of these variations is very limited ( $\bar{\zeta}_{int}]_{IMSA-Fuzzy} \in [10.5, 11.5]$  and  $\bar{\zeta}_{ext}]_{IMSA-Fuzzy} \in [0.2, 1.1]$ ).

Such an event seems to indicate a substantial invariance of the reconstruction effectiveness of the *IMSA – Fuzzy* versus the scatterer dimension. For comparison purposes, the same plots concerned with the standard *IMSA* are shown.

For completeness, the last experiment deals with a scenario (*Scenario 3*) characterized by an homogeneous ( $\tau = 3$ ) circular cylinder  $l$  in diameter with a significant noise level ( $SNR = 5\text{ dB}$ ) blurring the scattering data. Fig. 10 shows some inversion samples obtained without [Figs. 10(a)(c)] and with the *FLS* [Figs. 10(b)(d)] when  $l = 0.26 \lambda_0$  [Figs. 10(a)(b)] and  $l = 1.46 \lambda_0$  [Figs. 10(c)(d)]. Such results further confirm the effectiveness as well as the enhancement of the *FL*-based approach ( $\left. \frac{\bar{\zeta}_{tot} \rfloor_{IMSA}}{\bar{\zeta}_{tot} \rfloor_{IMSA-Fuzzy}} \right|_{\frac{l}{\lambda_0}=0.26} \simeq 6.9$  and  $\left. \frac{\bar{\zeta}_{tot} \rfloor_{IMSA}}{\bar{\zeta}_{tot} \rfloor_{IMSA-Fuzzy}} \right|_{\frac{l}{\lambda_0}=1.46} \simeq 4.34$ ) also in dealing with strong scatterers (beyond the “*weak scatterer*” condition).

#### 4.2.2 Experimental Validation

The last part of the numerical testing is devoted at assessing the effectiveness of the *IMSA – Fuzzy* technique when experimental scattering data are dealt with. Towards this end, the multiple-frequency angular-diversity bistatic data provided by the Institut Fresnel, Marseille, France [39] have been used as reference benchmark. The experimental imaging setup consists of a 2D bistatic measurement system with an emitter placed at a fixed position, while a receiver is rotating with an arm along the vertical axis of the cylindrical scatterer under test. Such a system allows to implement a multi-illumination/multi-view acquisition procedure characterized by  $V = 36$  views and  $M(v) = 49$ ,  $v = 1, \dots, V$ , sample measurement points.

The considered experimental dataset (“*dielTM\_dec8f.exp*”) is concerned with an off-centered homogeneous circular cylinder  $d = 30\text{ mm}$  in diameter. Such an object is characterized by a nominal value of the object function equal to  $\tau(x, y) = 2.0 \pm 0.3$  and it is located at  $x_c = 0.0$ ,  $y_c = -30\text{ mm}$ . As far as the investigation domain  $D_{inv}$  is concerned, a square domain  $30 \times 30\text{ cm}^2$  has been assumed and because of the aspect-limited nature of the experimental setup, the complete set of measures has been used, but only mono-frequency data have been considered.

The first computational test has been performed by using the scattering data at  $f = 3\text{GHz}$ . Even though the retrieved distributions are smoothed versions of the actual profile [Figs. 11(a)-(b)], it is possible to clearly detect the object under test as well as its location and shape (Tab. III). As far as the comparison between the *IMSA* and the *IMSA - Fuzzy* is concerned, the *FL*-based approach allows one to obtain a more homogeneous representation of the dielectric profile under test. However, non-so-relevant differences can be observed and the improvement in the reconstruction accuracy are not as large as for synthetic test cases. Moreover, the computational costs required by the two approaches for reaching the stationary condition [13] appear almost equivalent as shown in Fig. 12(a).

Such a behavior can be justified by a better *SNR* (greater than that of previous synthetic test cases) for the low-frequency scattering data when collected in a controlled-environment (as pointed out in [40]). On the other hand, it is well known that an enhanced corruption of the scattering data occur as the frequency increases.

In order to verify such a hypothesis, some reconstructions at higher frequencies ( $f = 6\text{GHz}$  and  $f = 8\text{GHz}$ ) have been carried out and the results are shown in Figs. 11(c)-11(f). As shown in [13], the reconstruction accuracy reduces apart from the *IMSA* strategy used. However, because of the decreasing of the *SNR* in correspondence with the increasing of  $f$ , the improvement in the reconstruction allowed by the *FLS* is considerable in terms of both quantitative imaging [Fig. 11(c) vs. Fig. 11(d) and Fig. 11(e) vs. Fig. 11(f) - Tab. III] and convergence rate [Figs. 12(b)-(c)].

## 5 Conclusions

In this paper, an innovative technique that integrates the iterative multi-scaling approach with an automatic strategy for estimating the uncertainty associated with the results of scattering measurements has been developed for microwave imaging purposes. By considering a multi-resolution representation of the profile under test, the proposed methodology allows one to yield a reliable reconstruction by means of the exploitation of the informa-

tion content available from noisy-corrupted scattering data. Towards this end, a fuzzy-logic-based decision strategy has been adopted in order to associate to each scattering sample a degree of “reliability”.

The main features of the proposed system are the following:

- capability to estimate the uncertainty associated with scattering measurements in an automatic fashion (allowing a “*transparent*” behavior when noise levels are negligible) thanks to the *FL*-based decision strategy;
- capability to exploit the amount of information collectable from scattering data thanks to a multi-resolution representation of the dielectric profile of the object under test;
- reduction of the computational costs thanks to the integration of the multi-scaling reconstruction scheme and the *FL* approach;
- robustness to corrupted data and noise;
- capability to deal with complex nonlinear cost functions.

Concerning the methodological novelties of this work, besides the definition of the global architecture of the whole system, they mainly rely on the combination of the innovative *FL*-based decision scheme within the multiresolution inversion architecture in order to contemporaneously and fully exploit limited and noisy scattering data characterized by an *a-priori* unknown degree of reliability.

In the numerical assessment, carried out on different conditions and datasets concerned with various scattering configurations and data (synthetic as well as experimental), the proposed architecture proved effective, providing both acceptable reconstruction accuracy and robustness to the noise. Final reconstructions have usually shown a general agreement with actual profiles and they confirm the enhanced inversion accuracy (compared to the state-of-the-art approaches) in correspondence with a decreasing of the *SNR*. Moreover, the numerical results pointed out that, as requested, the *FL*-based inversions are very

close and essentially identical to those obtained with a standard multi-resolution approach in the presence of low (or negligible) levels of noise.

Because of the preliminary positive results and the favorable trade-off between complexity/costs and reconstruction effectiveness, the proposed approach seems a promising tool to be extended to layered/stratified media as well as inhomogeneous backgrounds for dealing with biomedical and more realistic industrial applications where the reliability of scattering data is a critical key-issue.

## Acknowledgements

A. Massa wishes to thank E. Vico and M. Repetto for their support. Moreover, the authors are grateful to Ing. D. Franceschini for useful discussions.

This work has been partially supported in Italy by the *Center of REsearch And Telecommunication Experimentations for NETworked communities* (CREATE-NET).

## References

- [1] Special Issue on “Microwave imaging and inverse scattering techniques,” *J. Electromagn. Waves Applicat.*, vol. 17, Apr. 2003.
- [2] A. C. Dubey *et al.*, *Detection technology for mines and minelike targets*. Eds. Orlando, FL, 1995.
- [3] Q. Fang, P. M. Meaney, and K. D. Paulsen, “Microwave imaging reconstruction of tissue property dispersion characteristics utilizing multiple-frequency information,” *IEEE Trans. Microwave Theory Tech.*, vol. 52, pp. 1866-1875, Aug. 2004.
- [4] J. C. Bolomey and C. Pichot, “Microwave tomography: from theory to practical imaging systems,” *Int. J. Imag. Sys. Tech.*, vol. 2, pp. 144-156, 1990.
- [5] M. Bertero and P. Boccacci, *Introduction to Inverse Problems in Imaging*. IOP Publishing Ltd, Bristol, 1998.

- [6] O. M. Bucci and T. Isernia, "Electromagnetic inverse scattering: Retrievable information and measurement strategies," *Radio Sci.*, vol. 32, pp. 2123-2138, Nov.-Dec. 1997.
- [7] O. M. Bucci, L. Crocco, T. Isernia, and V. Pascazio, "Subsurface inverse scattering problems: Quantifying qualifying and achieving the available information," *IEEE Trans. Geosci. Remote Sensing*, vol. 39, pp. 2527-2537, Nov. 2001.
- [8] P. M. van den Berg and R. E. Kleinman, "A contrast source inversion method," *Inv. Probl.*, vol. 13, pp. 1607-1620, 1997.
- [9] L. Garnero, A. Franchois, J.-P. Hugonin, Ch. Pichot, and N. Joachimowicz, "Microwave imaging-complex permittivity reconstruction by simulated annealing," *IEEE Trans. Microwave Theory Tech.*, vol. 39, pp. 1801-1807, 1991.
- [10] S. Caorsi, A. Massa, and M. Pastorino, "A computational technique based on a real-coded genetic algorithm for microwave imaging purposes," *IEEE Trans. Geosci. Remote Sensing*, vol. 38, no. 4, pp. 1697-1708, 2000.
- [11] E. L. Miller and A. Willsky, "A multiscale, statistically based inversion scheme for linearized inverse scattering problems," *IEEE Trans. Geosci. Remote Sensing*, vol. 34, pp. 346-357, Mar. 1996.
- [12] A. Baussard, E. L. Miller, and D. Lesselier, "Adaptive multiscale reconstruction of buried objects," *Inverse Problems*, Special section on "Electromagnetic characterization of buried obstacles", W.C. Chew and D. Lesselier eds., vol. 20, pp. S1-S15, 2004.
- [13] S. Caorsi, M. Donelli, and A. Massa, "Detection, location, and imaging of multiple scatterers by means of the iterative multiscaling method," *IEEE Trans. Microwave Theory Tech.*, vol. 52, pp. 1217-1228, Apr. 2004.
- [14] R. Bhargava, and I.W. Levin, "Effective time averaging of multiplexed measurements: a critical analysis," *Anal. Chem.*, 74, pp. 1429-1435, 2002.

- [15] S. Kondakci, "Efficiency evaluation of the averaging noise reduction system," *Proc. EMBS International Conf.*, pp. 1958-1961, Oct. 2001.
- [16] Y.-C. Jenq, "Discrete-time method for signal and noise measurement," *Proc. IEEE Instrum. Meas. Technol. Conf.*, 24-26, pp. 68-71, April 1995.
- [17] A. Franchois and Ch. Pichot, "Microwave imaging - Complex permittivity reconstruction with a Levenberg-Marquardt method," *IEEE Trans. Antennas Propagat.*, vol. 45, pp. 203-215, 1997.
- [18] E. Bort, M. Donelli, A. Martini, and A. Massa, "An adaptive regularization strategy for microwave imaging problems," *IEEE Trans. Antennas Propagat.*, vol. 53, pp. 1858-1862, May 2005.
- [19] A. Casagrande, D. Franceschini, and A. Massa, "Assessment of the reliability and exploitation of the information content of inverse scattering data through a fuzzy-logic-based strategy - Preliminary results," *IEEE Trans. Geosci. Remote Sensing Lett.*, vol. 2, pp. 36-39, Jan. 2005.
- [20] L. A. Zadeh, "Fuzzy Sets," *Information and Control*, vol. 8, pp. 338-353, 1965.
- [21] S. Dutta, "Fuzzy logic applications: technological and strategic issues," *IEEE Trans. Eng. Manage.*, vol. 40, pp. 237-254, Aug. 1993.
- [22] L. X. Wang, *Adaptive Fuzzy Systems and Control - Design and Stability Analysis*. Englewood Cliffs, NJ: Prentice-Hall, 1994.
- [23] F. C. Morabito and E. Coccorese, "A fuzzy modelling approach for the solution of an inverse electrostatic problem," *IEEE Trans. Magn.*, vol. 32, no. 3, pp. 1330-1333, May 1996.
- [24] M. Chiampì, C. Ragusa and M. Repetto, "Fuzzy approach for multiobjective optimization in magnetics," *IEEE Trans. Magn.*, vol. 32, no. 3, pp. 1234-1237, May 1996.

- [25] Y. Tsuchida and M. Enokizono, "Fuzzy regularization method for ill-posed problems on ECT with Laplace transform BEM," *IEEE Trans. Magn.*, vol. 36, no. 4, pp. 1158-1162, July 2000.
- [26] J. H. Richmond, "Scattering by a dielectric cylinder of arbitrary cross section shape," *IEEE Trans. Antennas Propagat.*, vol. 13, pp. 334-341, 1965.
- [27] L. A. Zadeh, "Outline of a new approach to the analysis of complex systems and decision processes," *IEEE Trans. Syst., Man, Cybern.*, vol. 2, pp. 28-44, 1973.
- [28] L. A. Zadeh, "Fuzzy logic and approximate reasoning," *Synthese*, vol. 30, pp. 407-428, 1975.
- [29] R. R. Yager *et. al.*, *Fuzzy Sets and Applications: Selected papers by L. A. Zadeh*. Wiler-Interscience, New York, 1987.
- [30] K. Hirota, *Industrial Applications of Fuzzy Technology*. Springer-Verlag, New York, 1993.
- [31] D. Dubois and H. Prade, *Fuzzy Sets and Systems: Theory and Applications*. Academic, Orlando, 1980.
- [32] C. C. Lee, "Fuzzy logic in control systems: fuzzy logic controller, part I-II," *IEEE Trans. Syst., Man, and Cybern.*, vol. 20, pp. 404-435, 1990.
- [33] J. M. Mendel, "Fuzzy logic system for engineer - A tutorial," *Proc. IEEE*, vol. 83, pp. 345-377, March 1995.
- [34] H. Hellendoorn and C. Thomas, "Defuzzification in fuzzy controllers," *J. Intell. Fuzzy Syst.*, vol. 1, pp. 109-123, 1993.
- [35] E. Cox, "Fuzzy fundamentals," *IEEE Spectr.*, vol. 3, pp. 58-61, Oct. 1992.
- [36] A. Homaifar and E. McCormick, "Simultaneous design of membership functions and rule sets for fuzzy controllers using genetic algorithm," *IEEE Trans. Fuzzy Syst.*, vol. 3, pp. 129-139, May 1995.

- [37] H. S. Hwang, "Automatic design of fuzzy rule base for modelling and control using evolutionary programming," *IEEE Proc.-Control Theory Appl.*, vol. 146, pp. 9-16, Jan. 1999.
- [38] A. N. Tikhonov and V. Y. Arsenin, *Solution of Ill-Posed Problems*. Washington, DC: Winston, 1977.
- [39] K. Belkebir, S. Bonnard, F. Sabouroux, and M. Saillard, "Validation of 2D inverse scattering algorithms from multi-frequency experimental data," *J. Electromagn. Waves Appl.*, vol. 14, pp. 1637-1668, Dec. 2000.
- [40] M. Testorf and M. Fiddy, "Imaging from real scattered field data using a linear spectral estimation technique," *Inverse Problems*, vol. 17, pp. 1645-1658, Dec. 2001.

## Figure Captions

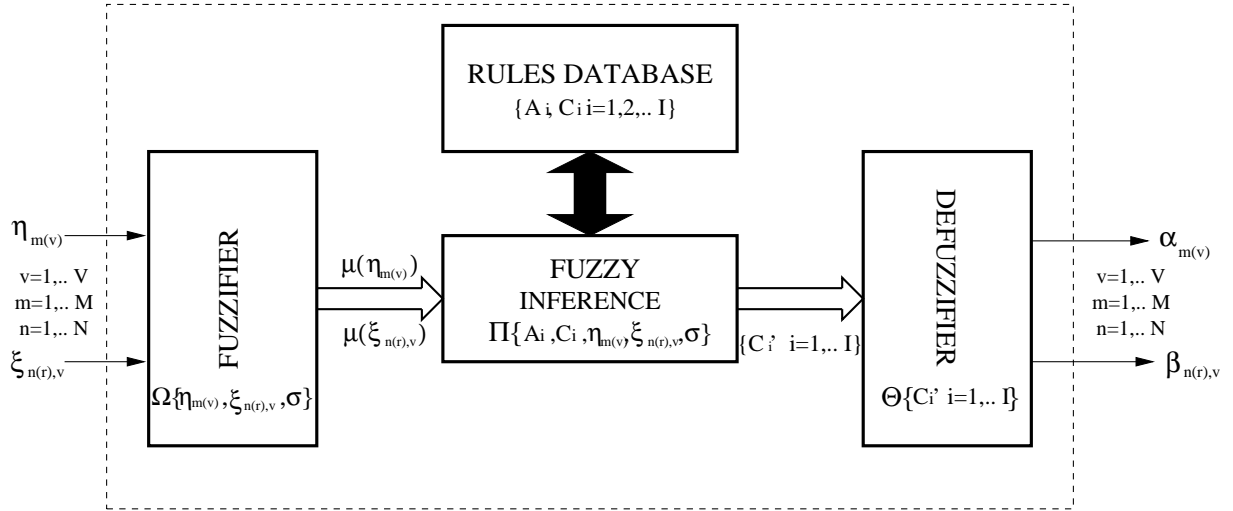
- **Figure 1.** (a) Block diagram of the *FLS*. (b) System architecture of the *FL*-based Approach.
- **Figure 2.** Antecedents (left) and consequences (right). Pictorial representation of the set of rules (a)(b) #1, (c)(d) #2, (e)(f) #3, (g)(h) #4, and (i)(l) #5.
- **Figure 3.** *FLS* Calibration (Scenario 1 -  $SNR = 5\text{ dB}$ ). Behaviors of the error indexes ( $\bar{\zeta}_j$ ,  $j = tot, int, ext$ ) versus the value of the variance  $\sigma$  of the fuzzification Gaussian membership function.
- **Figure 4.** Reconstruction of an off-centered square ( $l = 1.2\lambda_0$ ) homogeneous dielectric ( $\tau = 1.5$ ) cylinder - Samples of the dielectric profiles reconstructed by using the *IMSA* (left column) and the *IMSA - Fuzzy* method (right column): (a)(b)  $SNR = 20\text{ dB}$ , (c)(d)  $SNR = 10\text{ dB}$ , and (e)(f)  $SNR = 5\text{ dB}$ .
- **Figure 5.** Reconstruction of an off-centered square ( $l = 1.2\lambda_0$ ) homogeneous dielectric ( $\tau = 1.5$ ) cylinder - Average values of the error figures versus  $SNRs$ : (a)

localization error  $\bar{\delta}$ , (b) area-estimation error  $\bar{\Delta}$ , (c) total reconstruction error  $\bar{\zeta}_{tot}$ , (d) internal reconstruction error  $\bar{\zeta}_{int}$ , and (e) external reconstruction error  $\bar{\zeta}_{ext}$ .

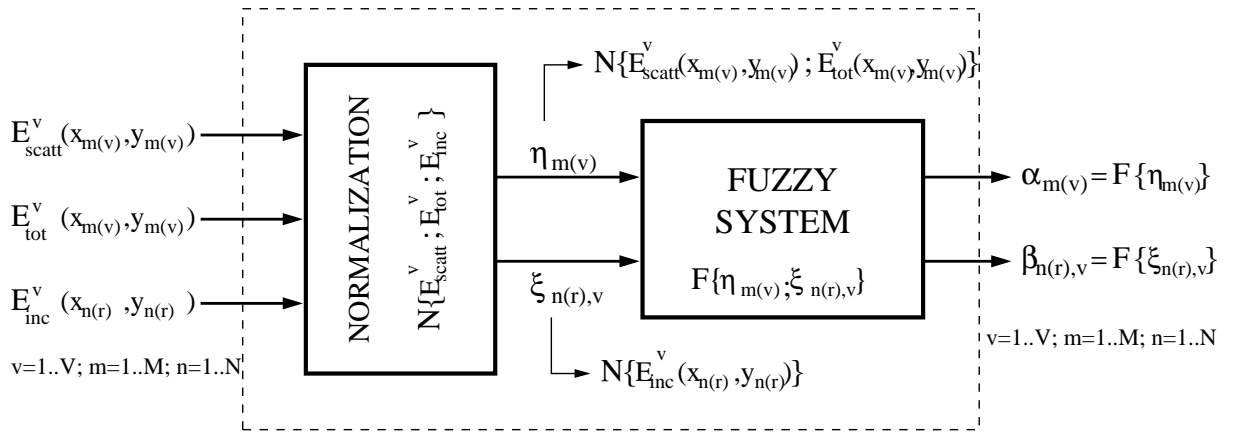
- **Figure 6.** Reconstruction of an off-centered square ( $l = 1.2\lambda_0$ ) homogeneous dielectric ( $\tau = 1.5$ ) cylinder - Samples of the dielectric profiles reconstructed by using the *Tikhonov* (left column) and the (b) *Landweber* (right column) regularization methods: (a)(b)  $SNR = 20\text{ dB}$ , (c)(d)  $SNR = 10\text{ dB}$ , and (e)(f)  $SNR = 5\text{ dB}$ . Born approach (Noiseless case) (g).
- **Figure 7.** Reconstruction of an off-centered square ( $l = 1.2\lambda_0$ ) homogeneous dielectric ( $\tau = 1.5$ ) cylinder - Behavior of the cost function during the multi-scaling minimization process: (a)  $SNR = 20\text{ dB}$ , (b)  $SNR = 10\text{ dB}$ , and (c)  $SNR = 5\text{ dB}$ .
- **Figure 8.** Reconstruction of an off-centered square ( $l = 1.2\lambda_0$ ) homogeneous dielectric ( $\tau = 1.5$ ) cylinder - Behavior of the convergence index  $\Delta K_{tot}$  versus  $SNR$ .
- **Figure 9.** Reconstruction of an off-centered square homogeneous dielectric ( $\tau = 1.5$ ) cylinder ( $SNR = 5\text{ dB}$ ) - Average values of the reconstruction error figures versus object side  $l$ : (a)  $\bar{\zeta}_{tot}$ , (b)  $\bar{\zeta}_{int}$ , and (c)  $\bar{\zeta}_{ext}$ .
- **Figure 10.** Reconstruction of an off-centered circular homogeneous dielectric ( $\tau = 3$ ) cylinder ( $SNR = 5\text{ dB}$ ) - Samples of the dielectric profiles reconstructed by using the *IMSA* (left column) and the *IMSA – Fuzzy* method (right column): (a)(b)  $\frac{l}{\lambda_0} = 0.26$  and (c)(d)  $\frac{l}{\lambda_0} = 1.46$ .
- **Figure 11.** Reconstruction of an off-centered homogeneous circular cylinder (Real dataset “Marseille” [39] - “*dielTM\_dec8f.exp*”). Dielectric distributions reconstructed at the convergence by means of (left column) the standard *IMSA* and (right column) the *IMSA – Fuzzy* method. (a)(b)  $f = 3\text{ GHz}$ , (c)(d)  $f = 6\text{ GHz}$ , and (e)(f)  $f = 8\text{ GHz}$ .
- **Figure 12.** Reconstruction of an off-centered homogeneous circular cylinder (Real dataset “Marseille” [39] - “*dielTM\_dec8f.exp*”). Behavior of the cost function during the multi-scaling minimization process: (a)  $f = 3\text{ GHz}$ , (b)  $f = 6\text{ GHz}$ , and (c)  $f = 8\text{ GHz}$ .

## Table Captions

- **Table I.** *FLS* Calibration - Set of rules. Average values of the error indexes ( $\bar{\zeta}_j$ ,  $j = tot, int, ext$ ) for different sets of rules when  $SNR = 5 dB$  for (a) *Scenario 1* and (b) *Scenario 2*.
- **Table II.** Reconstruction of an off-centered square ( $l = 1.2 \lambda_0$ ) homogeneous dielectric ( $\tau = 1.5$ ) cylinder - Average reconstruction errors ( $\bar{\zeta}_{tot}$ ,  $\bar{\zeta}_{int}$ , and  $\bar{\zeta}_{ext}$ ) obtained by the *IMSA* and *IMSA - Fuzzy* for different values of  $SNR$ .
- **Table III.** Reconstruction of an off-centered homogeneous circular cylinder (Real dataset “Marseille” [39] - “*dielTM\_dec8f.exp*”). Actual and estimated scatterer parameters ( $f = 3 GHz$ ,  $f = 6 GHz$ , and  $f = 8 GHz$ ).



(a)



(b)

Fig. 1 - M. Benedetti *et al.*, “An adaptive multi-scaling imaging technique ...”

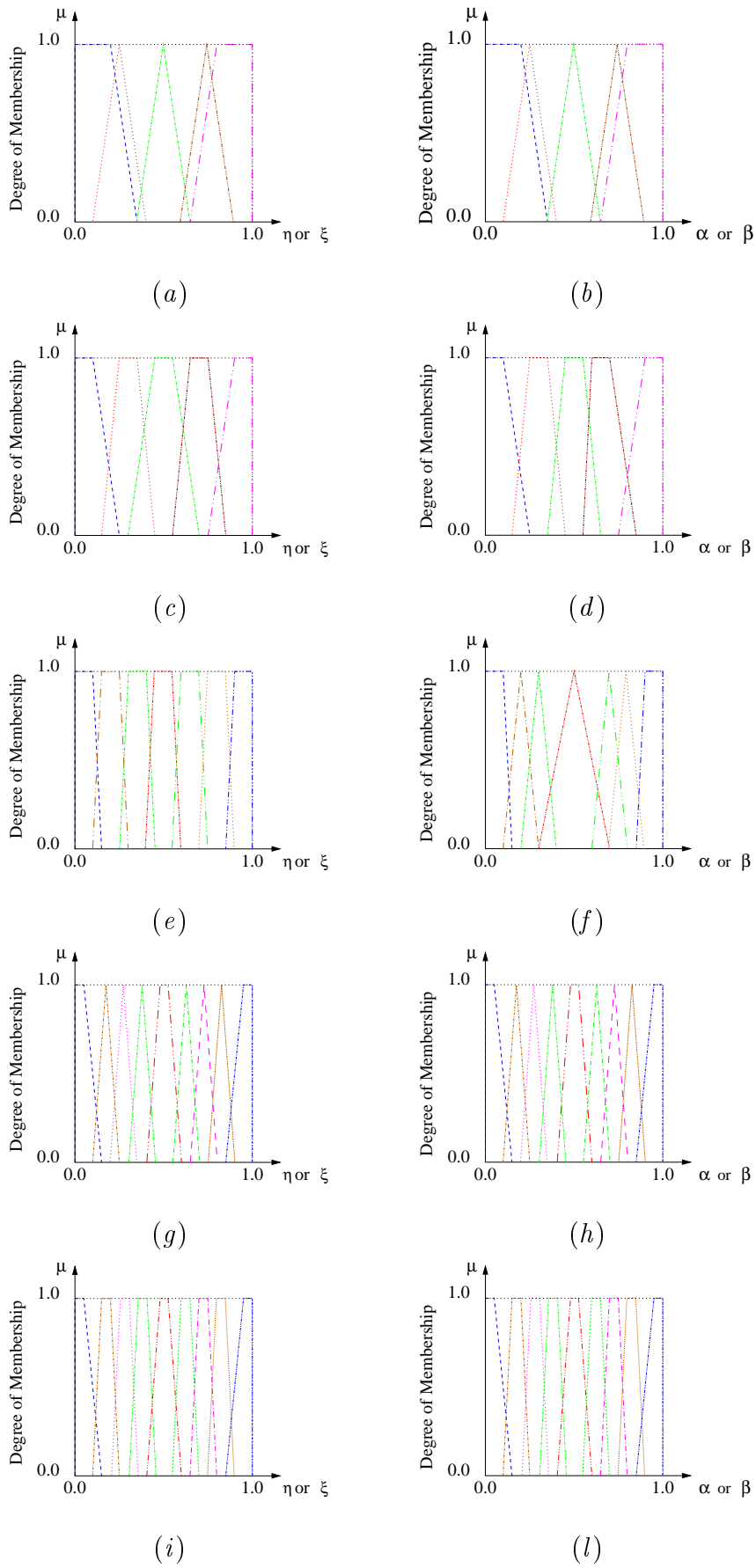


Fig. 2 - M. Benedetti *et al.*, “An adaptive multi-scaling imaging technique ...”

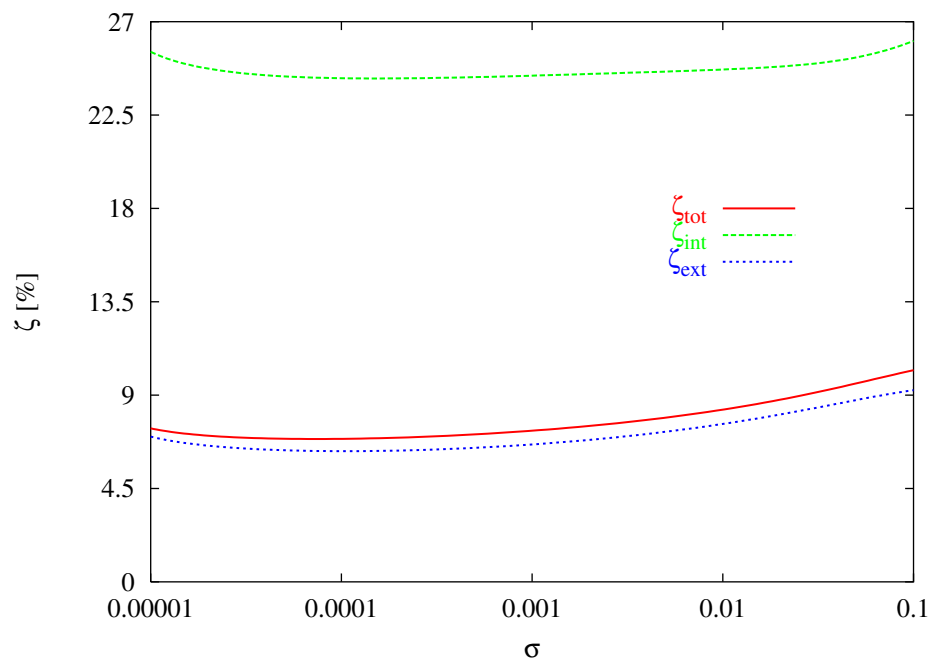


Fig. 3 - M. Benedetti *et al.*, “An adaptive multi-scaling imaging technique ...”

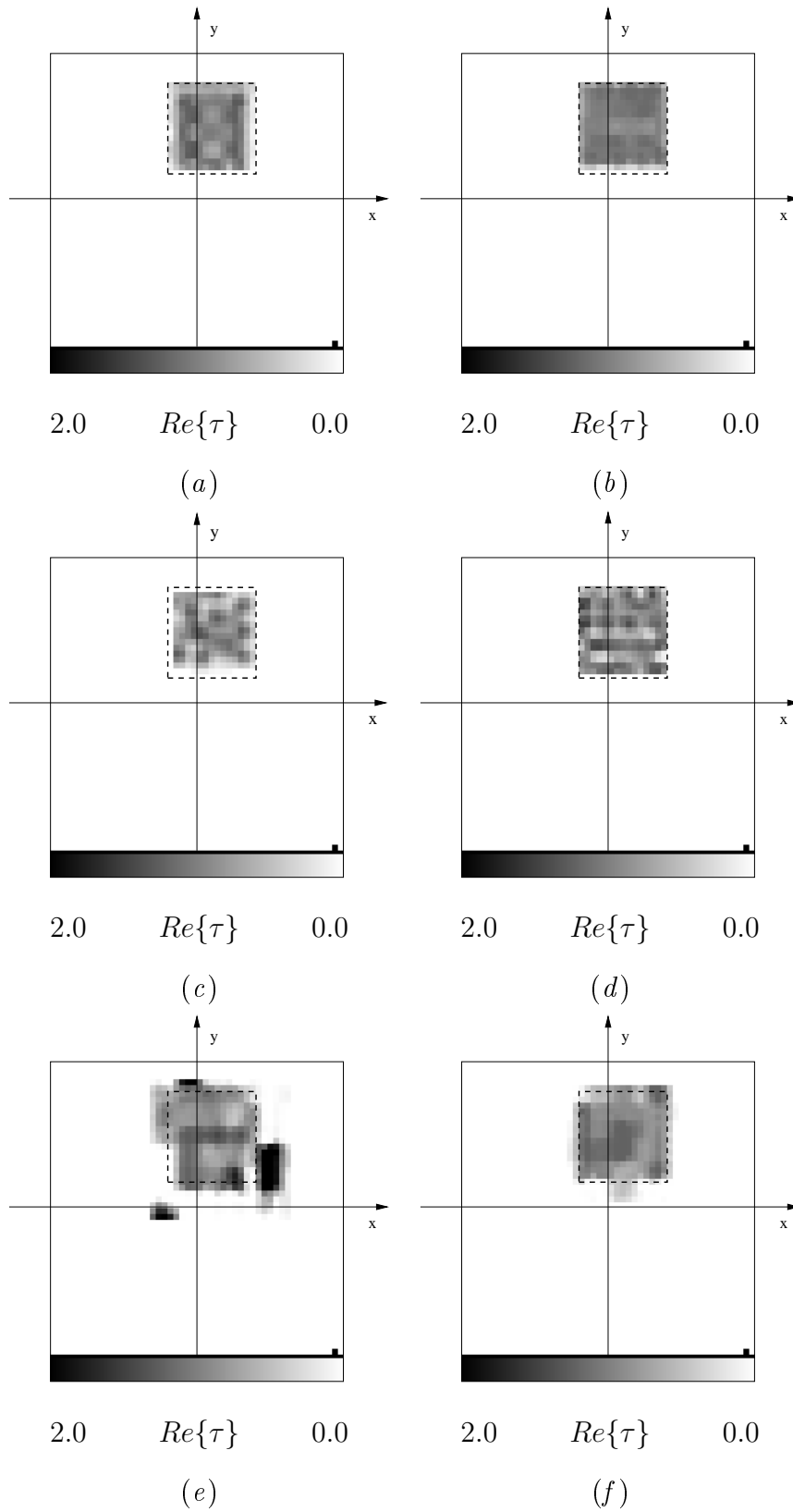
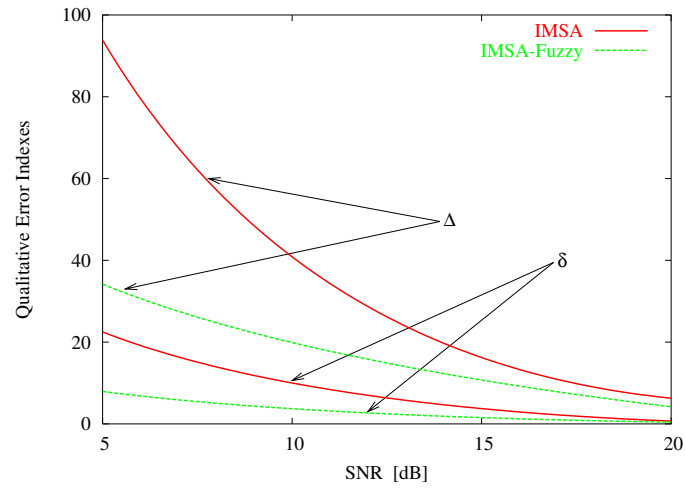
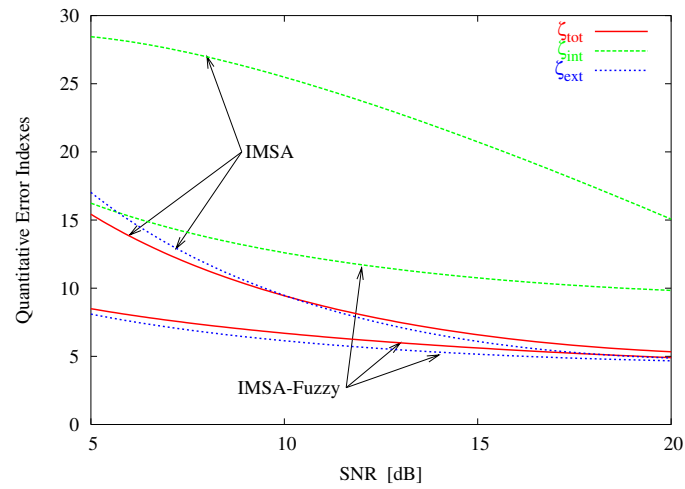


Fig. 4 - M. Benedetti *et al.*, “An adaptive multi-scaling imaging technique ...”



(a)



(b)

Fig. 5 - M. Benedetti *et al.*, "An adaptive multi-scaling imaging technique ..."

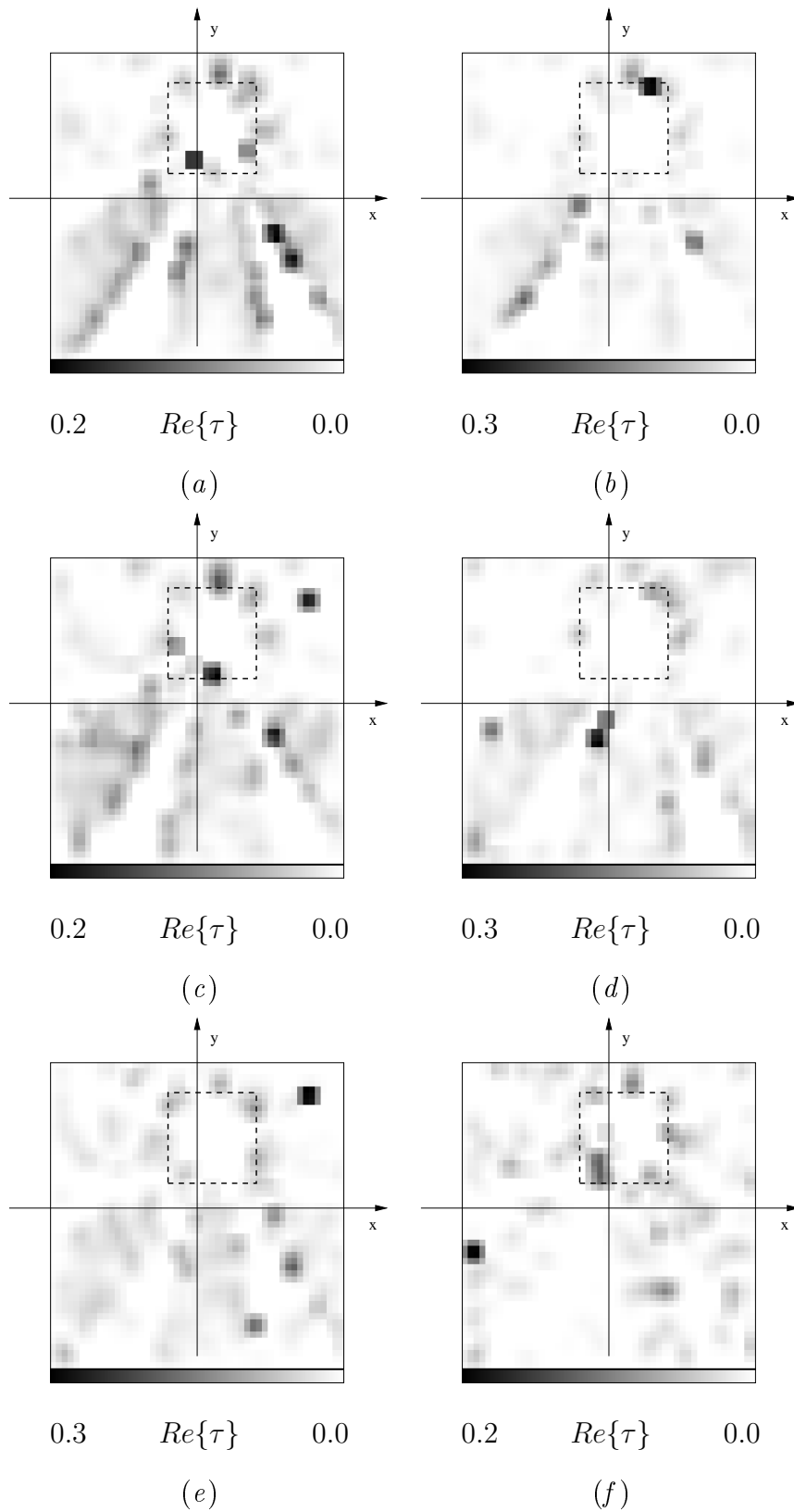


Fig. 6(I) - M. Benedetti *et al.*, “An adaptive multi-scaling imaging technique ...”

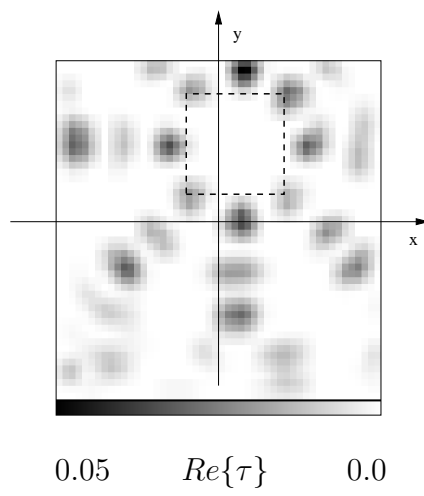
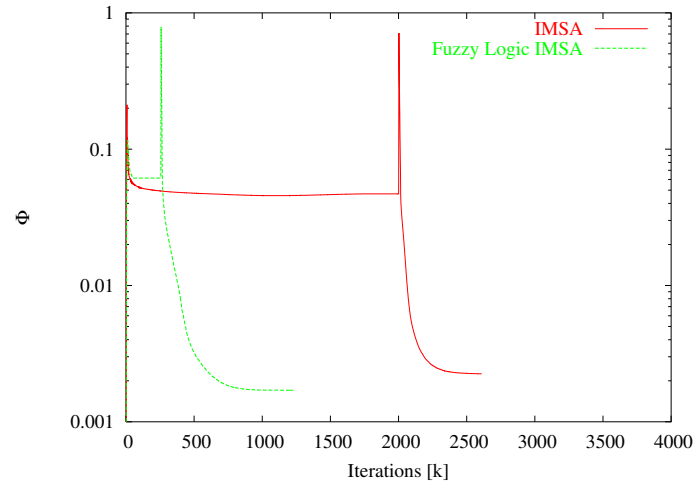
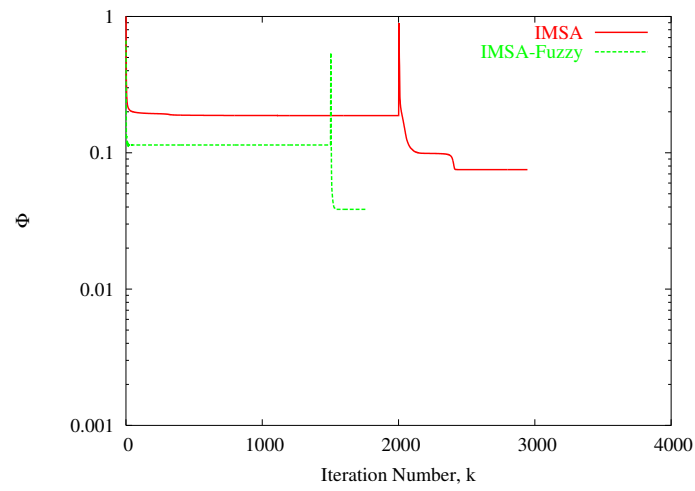


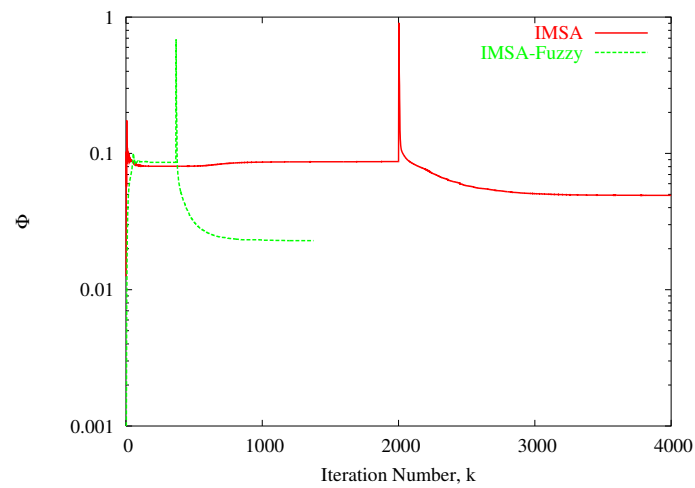
Fig. 6(II) - M. Benedetti *et al.*, "An adaptive multi-scaling imaging technique ..."



(a)



(b)



(c)

Fig. 7 - M. Benedetti *et al.*, “An adaptive multi-scaling imaging technique ...”

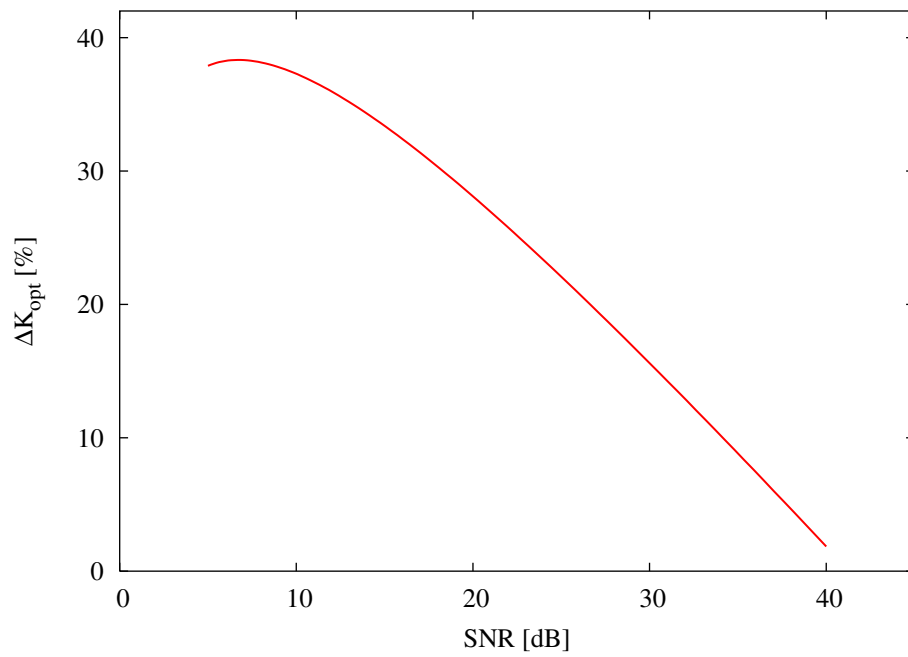


Fig. 8 - M. Benedetti *et al.*, “An adaptive multi-scaling imaging technique ...”

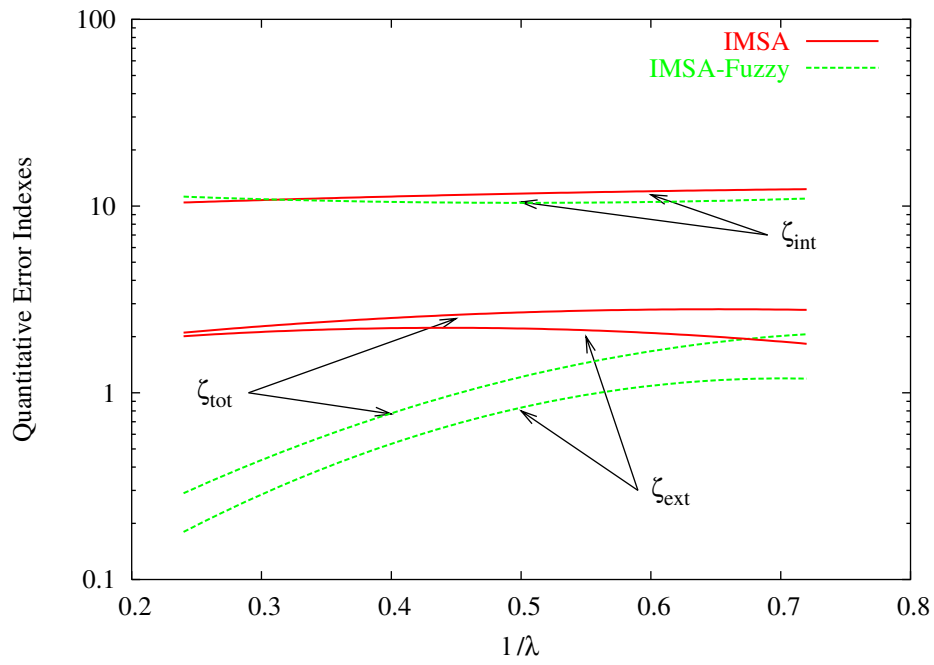


Fig. 9 - M. Benedetti *et al.*, “Microwave imaging technique based on ...“

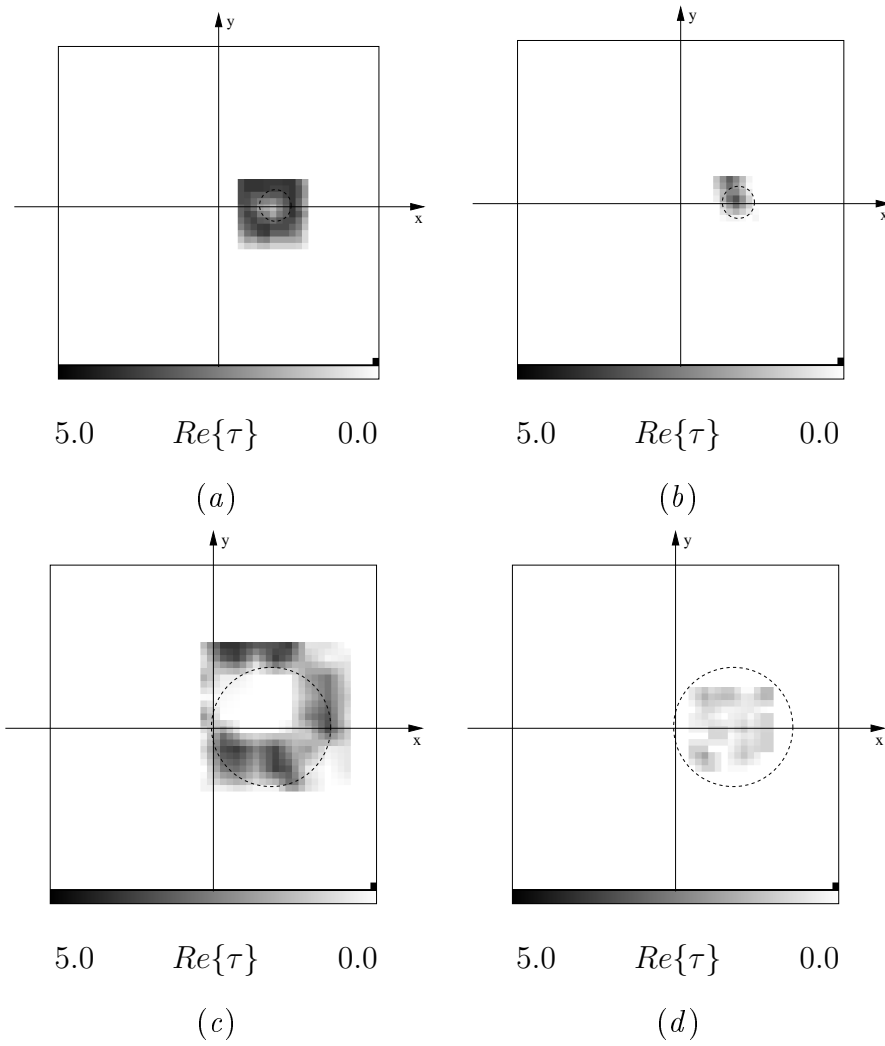


Fig. 10 - M. Benedetti *et al.*, “ An adaptive multi-scaling imaging technique ...”

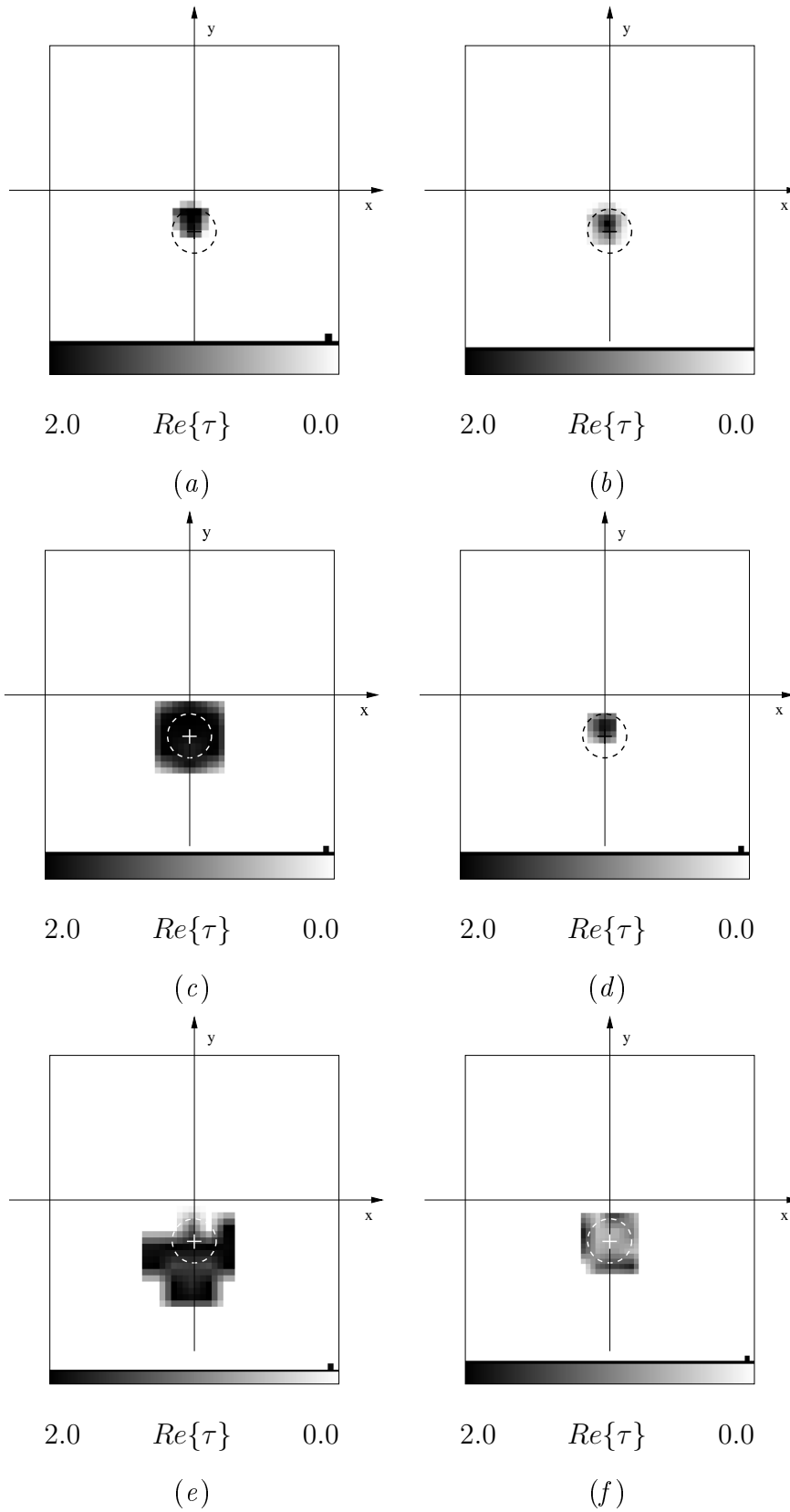
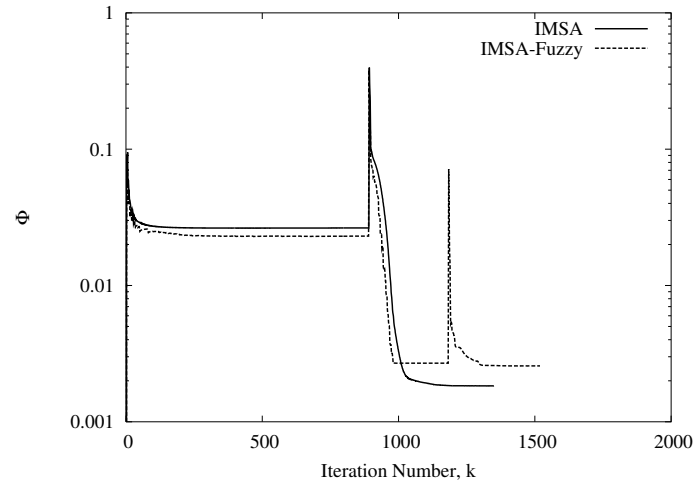
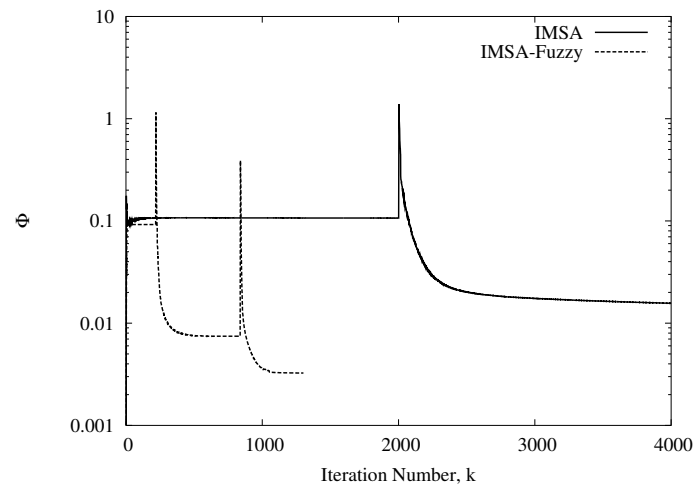


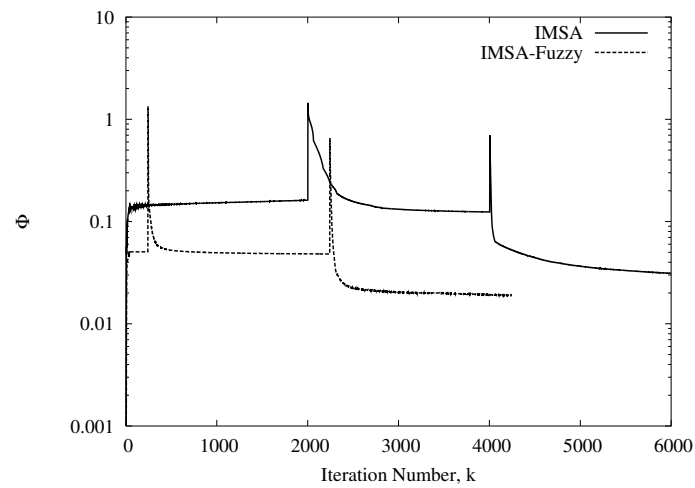
Fig. 11 - M. Benedetti *et al.*, “An adaptive multi-scaling imaging technique ...”



(a)



(b)



(c)

Fig. 12 - M. Benedetti *et al.*, “An adaptive multi-scaling imaging technique ...”

<i>Set of Rules</i>	$\bar{\zeta}_{tot}$	$\bar{\zeta}_{int}$	$\bar{\zeta}_{ext}$
#1	5.73	19.55	5.20
#2	6.97	18.85	6.47
#3	5.63	18.24	5.05
#4	6.06	26.18	5.22
#5	7.15	22.22	6.52

(a)

<i>Set of Rules</i>	$\bar{\zeta}_{tot}$	$\bar{\zeta}_{int}$	$\bar{\zeta}_{ext}$
#1	10.00	32.62	8.39
#2	9.56	30.86	8.30
#3	9.01	28.29	7.69
#4	9.56	32.57	8.00
#5	9.36	29.31	7.95

(b)

Tab. I - M. Benedetti *et al.*, “An adaptive multi-scaling imaging technique ...”

	<i>SNR = 20 dB</i>		<i>SNR = 10 dB</i>		<i>SNR = 5 dB</i>	
<i>Errors</i>	<i>IMSA</i>	<i>IMSA Fuzzy</i>	<i>IMSA</i>	<i>IMSA Fuzzy</i>	<i>IMSA</i>	<i>IMSA Fuzzy</i>
$\bar{\zeta}_{tot}$	5.98	5.45	6.18	6.17	14.49	8.07
$\bar{\zeta}_{int}$	11.78	10.40	11.63	8.09	10.84	8.77
$\bar{\zeta}_{ext}$	5.77	5.16	6.09	5.92	14.66	8.03

Tab. II - M. Benedetti *et al.*, "An adaptive multi-scaling imaging technique ..."

	$\frac{x_c}{\lambda_0}$	$\frac{y_c}{\lambda_0}$	$\frac{L_{RoI}}{2\lambda_0}$
$f = 3 \text{ GHz}$			
<i>Actual</i>	0.0	-0.30	0.150
<i>IMSA Fuzzy</i>	0.02	-0.27	0.144
<i>IMSA</i>	0.02	-0.27	0.140
$f = 6 \text{ GHz}$			
<i>Actual</i>	0.0	-0.60	0.30
<i>IMSA Fuzzy</i>	0.03	-0.52	0.33
<i>IMSA</i>	0.02	-0.68	0.74
$f = 8 \text{ GHz}$			
<i>Actual</i>	0.0	-0.80	0.40
<i>IMSA Fuzzy</i>	0.0	-0.95	0.91
<i>IMSA</i>	-0.16	-1.08	1.43

Tab. III - M. Benedetti *et al.*, “An adaptive multi-scaling imaging technique ...”